

To cite this document:

H.Ciardo, B. Lecampion, F. Fayard, S. Chaillat "A fast boundary element based solver for localized inelastic deformations"

***Int. J. Numer. Meth. Engng* 121:5696-5718 (2020)**

<https://doi.org/10.1002/nme.6520>

A fast boundary element based solver for localized inelastic deformations

F. Ciardo^a, B. Lecampion^{a,*}, F. Fayard^b, S. Chaillat^c

^a*Geo-Energy Lab - Gaznat chair in Geo-Energy, EPFL, ENAC-IIC-GEL, Lausanne, Switzerland*

^b*Inside Loop, France*

^c*POEMS (CNRS-ENSTA Paris-INRIA), ENSTA Paris, Institut Polytechnique de Paris, France*

Abstract

We present a numerical method for the solution of non-linear geo-mechanical problems involving localized deformation along shear bands and fractures. We leverage the boundary element method to solve for the quasi-static elastic deformation of the medium while rigid-plastic constitutive relations govern the behavior of displacement discontinuity (DD) segments capturing localized deformations. A fully implicit scheme is developed using a hierarchical approximation of the boundary element matrix. Combined with an adequate block pre-conditioner, this allows to tackle large problems via the use of an iterative solver for the solution of the tangent system. Several two-dimensional examples of the initiation and growth of shear-bands and tensile fractures illustrate the capabilities and accuracy of this technique. The method does not exhibit any mesh dependency associated with localization provided that i) the softening length-scale is resolved and ii) the plane of localized deformations is discretized a-priori using DD segments.

Keywords: Shear bands, Fractures, Boundary element, hierarchical matrix

1. Introduction

1 Driven by geomechanical applications such as faulting, shear-banding and
2 fracturing typically occurring in large domains, we develop a computational
3 method for the solution of two dimensional problems exhibiting localized
4

*brice.lecampion@epfl.ch

5 inelastic deformations. We use the boundary element method for the solu-
6 tion of quasi-static elasticity in the medium and accounts for the presence
7 of potential displacement discontinuity (DD) segments where inelastic defor-
8 mations take place. We use a rigid-plastic like constitutive relation for these
9 DD segments. In particular, we combine a non-associated Mohr-Coulomb
10 frictional behavior with a tensile cut-off, allowing for softening of cohesion,
11 friction and tensile strength. Although the method can be further coupled
12 with fluid flow, we restrict here for clarity to the case where mechanical
13 deformation does not affect flow.

14 Elasto-plastic problems leading to localized plastic deformations have
15 been extensively investigated using both finite element (FEM) [1, 2, 3, 4]
16 and boundary element (BEM) [5, 6] where in the latter plastic defor-
17 mations are accounted for via volume integral terms (thus requiring a bulk dis-
18 cretization of the plastic zones [7]). The numerical solutions of this class
19 of non-linear boundary value problems typically exhibit mesh dependen-
20 cies which are the results of the non-uniqueness associated with the bifur-
21 cation of the underlying continuum problem¹ [8]. Several remedies have
22 been proposed to overcome these difficulties: i) introduction of material rate
23 dependence [9, 10] which in effect introduce a length-scale, ii) incorporation
24 of a material length-scale in the material constitutive response via gradient
25 based theories [11, 12, 13], non local models [14] or Cosserat continua [15].

26 In this contribution, we adopt a different approach. Namely, we hypoth-
27 esise that inelastic deformations can only be localized along displacement
28 discontinuity segments and express the yielding criteria and flow rule only
29 along these segments. This approach shares similarities with cohesive zone
30 modeling in FEM where cohesive traction-separation law between interface
31 element control crack growth [16, 17, 18, 19] and can be traced back to
32 Palmer and Rice [20] for shear band growth. It also resembles the discrete
33 dislocation plasticity method [21]. The use of a boundary element method for
34 the discretization of the DD segments allows to efficiently resolve potential
35 localization phenomena without extensive bulk domain discretization. This
36 is particularly attractive for large domain. Moreover the DD segments are
37 rigid if not at yield thus recovering a solely elastic response in that limit.

38 In the following, we first present the mathematical formulation of this

¹Strain-softening and non-associated is not necessary in tri-axial setting for localization to occur.

39 method restricting to a plane strain configuration. The numerical scheme
 40 devised as well as the choice of an adequate pre-conditioner for the iterative
 41 solution of the resulting tangent system is then discussed in details. We
 42 finally illustrate the accuracy and capabilities of this approach on a series
 43 of examples involving the initiation and growth of shear-bands and tensile
 44 cracks.

45 2. Problem formulation

46 We consider an homogeneous, isotropic and linear elastic medium under
 47 plane-strain condition. The medium is subjected to a generalized system
 48 of forces that may cause localized inelastic deformations along a set of pre-
 49 defined segments that translate into displacement discontinuities. A yield
 50 criterion controls the occurrence of displacement discontinuities along these
 51 segments. If the yield criterion is not satisfied on a particular segment, the
 52 displacement discontinuities are zero. Upon yielding, the evolution of dis-
 53 placement discontinuities is governed by a non-associated plastic like flow
 54 rule [22]. Incorporating softening, the formalism allows to recover cohesive
 55 zone like behavior as well as friction. This enable to capture localized defor-
 56 mations (shear bands, open and sliding fractures). The model is thus akin
 57 to a rigid plastic one for the potentially failing segments and elastic for the
 58 rest of the solid. This translates into an elasto-plastic response for the whole
 59 medium.

60 2.1. Elastic medium with displacement discontinuities

61 Due to the assumption that inelastic deformations are limited to displace-
 62 ment discontinuity segments, the use of boundary integral equations to solve
 63 for the quasi-static elastic balance of momentum is particularly appealing es-
 64 pecially for exterior problems. Referring to Figure 1, Γ denotes the locus of
 65 displacement discontinuities, located in a elastic domain $\Omega \in \mathbb{R}^2$ with an elas-
 66 tic stiffness tensor \mathbf{c}_{ijkl} . We denote the unit normal vector $n_i = n_i^- = -n_i^+$
 67 where n_i^+ and n_i^- are the unit normal vector of the top and bottom sur-
 68 faces of Γ respectively (see Fig. 1). The corresponding shear orthonormal
 69 vectors s follow the right-hand side rule. We use the convention of positive
 70 displacement discontinuities in opening, positive slip for clock-wise rotation
 71 of matter:

$$d_i = u_i^+ - u_i^- \quad (1)$$

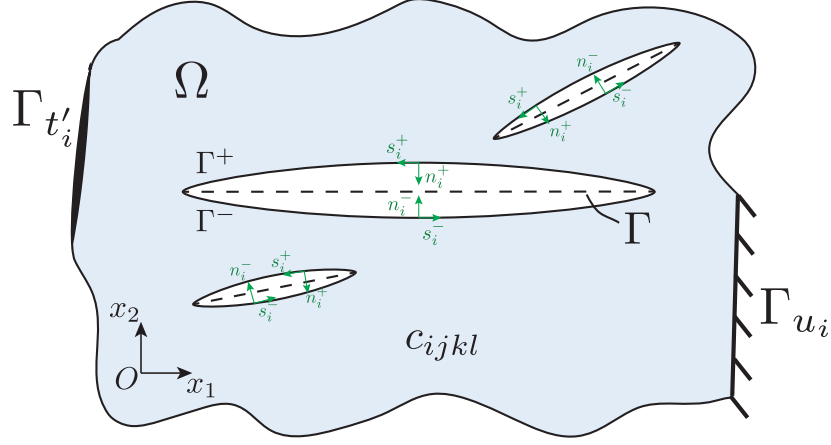


Figure 1: A linearly isotropic elastic medium Ω containing a set of pre-existing potential fractures and slip planes whose mid-plane are denoted by Γ . Boundary regions with prescribed displacements or effective traction are denoted respectively as Γ_{u_i} and $\Gamma_{t'_i}$.

72 where u_i is the displacement vector. On the other hand, following the con-
 73 vention of geo-mechanics, stresses are taken positive in compression.

74 The quasi-static elastic equilibrium is written as the following boundary
 75 integral equations, relating tractions and displacement discontinuities in the
 76 local normal (n) and tangential (s) frame along Γ [23]:

$$t_i(\mathbf{x}) - t_i^o(\mathbf{x}) = n_j(\mathbf{x}) \int_{\Gamma} c_{ijkl} \frac{\partial S_{ab}^k}{\partial \xi_l}(\mathbf{x}, \xi) d_a(\xi) n_b(\xi) d\xi \quad \text{for } \mathbf{x} \in \Gamma, i, j, = n, s, \quad (2)$$

77 where $t_i = \sigma_{ij} n_j$ is the traction vector, t_i^o is the initial traction and $S_{ab}^k(\mathbf{x}, \xi)$
 78 is the fundamental solution for the stresses at ξ induced by a point force
 79 located at \mathbf{x} along the k th direction. $c_{ijkl} \frac{\partial S_{ab}^k}{\partial \xi_l}(\mathbf{x}, \xi)$ corresponds to the stress
 80 induced by a dislocation dipole. We refer to [23, 7, 24] for more details and
 81 expressions for these fundamental elastic solutions. The integral equation
 82 (2) is hyper-singular but classical approaches are available in the literature
 83 if a collocation [25] or symmetric Galerkin technique [26] is used to drive the
 84 discretization.

85 2.2. Constitutive relations for displacement discontinuities segments

We use a Mohr-Coulomb criterion combined with a tensile cut-off as the yielding function for localized failure on segments, allowing for softening (see Figure 2). Accounting for the presence of fluid (of pressure p), we combine

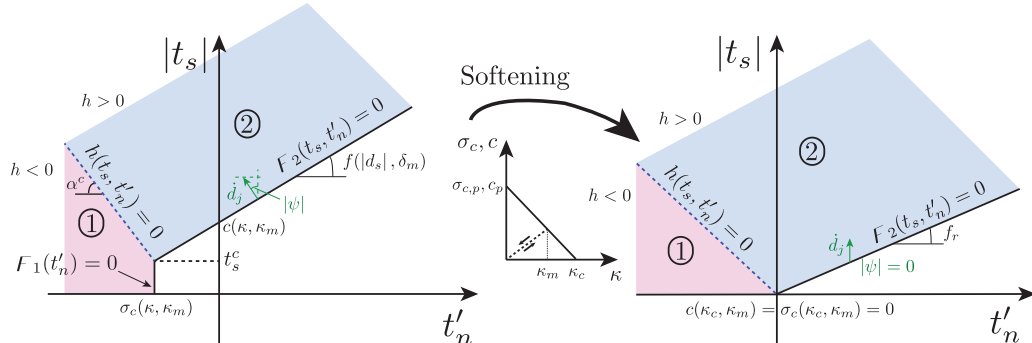


Figure 2: Composite yielding surface for displacement discontinuity segments combining a Mohr-Coulomb (region 2) with a tensile cut-off (region 1) - left panel. Softening of tensile strength, cohesion as well as friction is possible ultimately resulting in a purely frictional behavior at complete softening - right panel. A non-associated flow rule for the frictional response limit plastic dilatancy and result in critical state flow at complete softening (right).

two yield functions expressed in terms of the local components of effective traction vector $t'_n = t_n - p$, $t'_s = t_s$:

$$F_1(t'_n) = -\sigma_c(\kappa, \kappa_m) - t'_n \leq 0, \quad (3a)$$

$$F_2(t_s, t'_n) = |t_s| - c(\kappa, \kappa_m) - f(|d_s|, \delta_m)t'_m \leq 0, \quad (3b)$$

86 where $f(|d_s|, \delta_m)$ is the friction coefficient function of absolute value of shear
 87 slip d_s and the maximum slip obtained during the loading history δ_m . Sim-
 88 ilarly, $\sigma_c(\kappa, \kappa_m)$ and $c(\kappa, \kappa_m)$ are the tensile strength and cohesion respec-
 89 tively, both function of a softening variable $\kappa = \sqrt{\xi^2 d_s^2 + d_n^2}$, where $\xi > 0$
 90 is a phenomenological parameter accounting for the relative intensity of shear
 91 and normal displacement on softening. κ_m corresponds to the maximum
 92 value of κ obtained during the loading history.

93 In order to define uniquely which yield function the effective traction
 94 vector must satisfy when both criteria are violated simultaneously (when
 95 $F_1(t'_n) > 0$ and $F_2(t_s, t'_n) > 0$), we use a function $h(t_s, t'_n)$ similar to the one
 96 proposed in [27]

$$h(t_s, t'_n) = |t_s| - t_s^c - \alpha^c(\sigma_c(\kappa, \kappa_m) + t'_n), \quad (4)$$

97 where t_s^c and α^c are two scalars function of the current friction, cohesion and
 98 tensile strength defined as

$$t_s^c = c(\kappa, \kappa_m) - f(|d_s|, \delta_m) \sigma_c(\kappa, \kappa_m) \quad 99$$

$$\alpha^c = \sqrt{1 + f(|d_s|, \delta_m)^2} - f(|d_s|, \delta_m) \quad 100$$

101 The yielding functions $F_1(t'_n)$ and $F_2(t_s, t'_n)$ represent inequality constraints
 102 for the traction applied on Γ . Combined with the function $h(t_s, t'_n)$, they allow
 103 to split uniquely the effective traction space into admissible and inadmissible
 104 regions (see Figure 2): specifically, $F_2(t_s, t'_n)$ for $h(t_s, t'_n) \geq 0$ (shear failure)
 105 and $F_1(t'_n)$ for $h(t_s, t'_n) < 0$. In the following, we describe the relations that
 106 the local tractions must satisfy on a given displacement discontinuity segment
 107 Γ for the different inadmissible regions 1 and 2 of Figure 2 corresponding to
 108 tensile or shear failure respectively.

109 2.2.1. Shear failure

Shear failure is captured via a non-associated flow rule to better reproduce shear-induced dilatancy (with a dilatant angle typically lower than friction angle). The yield criteria constraint and corresponding evolution of the displacement discontinuity rates are thus similar to frictional contact with cohesion:

$$F_2(t_s, t'_n) < 0, \quad \dot{d}_s = 0, \quad \dot{d}_n = 0 \quad (5a)$$

$$F_2(t_s, t'_n) = 0, \quad \dot{d}_s = \left| \dot{d}_s \right| \text{sign}(t_s), \quad \dot{d}_n = \left| \dot{d}_s \right| \tan \psi(|d_s|, \delta_m) \quad (5b)$$

110 During shear failure, the evolution of cohesion c and friction coefficient
 111 f with non-linear deformations governs the traction separation along Γ . We
 112 assume that the cohesion c degrades linearly with softening variable κ in
 113 a similar way than the tensile strength σ_c (see the following sub-section)
 114 keeping the ratio c/σ_c constant. The friction coefficient f is supposed to
 115 weaken linearly with the absolute value of slip $|d_s|$, from a peak value f_p to
 116 a residual value f_r for slip larger than a critical slipping distance δ_c [20]:

$$f(|d_s|, \delta_m) = \begin{cases} f_p - \frac{f_p - f_r}{\delta_c} |d_s| & |d_s| < \delta_c \ \& \ |d_s| = \delta_m \\ f_p - \frac{f_p - f_r}{\delta_c} \delta_m & |d_s| < \delta_c \ \& \ |d_s| < \delta_m \\ f_r & |d_s| > \delta_c \end{cases} \quad (6)$$

117 Similarly, we assume that the dilatancy angle $\tan \psi$ softens linearly with
 118 cumulative slip $|d_s|$, from a peak value $\tan \psi_p$ down to zero above a critical
 119 slip distance δ_c at which a critical state is reached [28]. Like for the friction

120 coefficient, the dilatancy angle does not evolve along the unloading/reloading
 121 branch. Although one can expect a drop of dilation angle during reverse
 122 deformation (see Stupkiewicz and Mróz [29] for discussion), we stick to that
 123 assumption for sake of simplicity in the following.

124 2.2.2. Tensile failure

Tensile failure on Γ (inadmissible region 1 of Figure 2) is directly controlled by the value of the effective normal traction. The relations for the evolution of the displacement discontinuities are here given by:

$$F_1(t'_n) < 0, \quad \dot{d}_n = 0, \quad \dot{d}_s = 0 \quad (7a)$$

$$F_1(t'_n) = 0, \quad \left| \dot{d}_n \right| > 0, \quad \dot{d}_s = 0 \quad (7b)$$

125 with the complementary condition $F_1(t'_n) \left| \dot{d}_n \right| = 0$. The sign of \dot{d}_n depends
 126 on the loading / unloading sequence and results from the application of the
 127 constraint $F_1(t'_n) = 0$ in the solution of the balance of momentum.

128 The evolution of the critical tensile strength σ_c with softening variable κ
 129 governs the relation between tractions and displacement discontinuities along
 130 Γ in a similar way than in cohesive zone models of fracture [17, 30, 31]. In
 131 the following, we assume that σ_c softens linearly with κ , from a peak value
 132 $\sigma_{c,p}$ to zero when κ is larger than a critical value κ_c . We also account for a
 133 reversible linear unloading/re-loading branch when the softening variable κ
 134 is lower than its maximum value reached during the loading history κ_m (see
 135 Figure 2). This can be summarized as

$$\frac{\sigma_c(\kappa, \kappa_m)}{\sigma_{c,p}} = \begin{cases} 1 - \kappa/\kappa_c & \kappa < \kappa_c \ \& \ \kappa = \kappa_m \\ (1 - \kappa_m/\kappa_c)\kappa/\kappa_m & \kappa < \kappa_c \ \& \ \kappa < \kappa_m \\ 0 & \kappa > \kappa_c \end{cases} \quad (8)$$

136 At complete softening, both the tensile strength σ_c and the cohesion c
 137 are zero resulting in a purely frictional Mohr-Coulomb criterion (see Figure 2
 138 right). As a result, if $F_1(t'_n) = 0$ at complete softening (i.e. $t'_n = 0$), one must
 139 also enforce $t_s = 0$ (i.e. $F_2(t_s, t'_n) = 0$) and as a result $\left| \dot{d}_n \right| > 0$, $\left| \dot{d}_s \right| > 0$.

140 Non inter-penetrability constraint at closure

141 When the tensile mode I failure is active, the sign of the normal displacement
 142 discontinuity rate is the result of the elastic balance of momentum of the
 143 whole medium, boundary conditions and the associated interactions between

144 failed segments. Upon unloading, crack closure is possible. Of course, the
 145 internal crack surfaces can not interpenetrate. Accounting for the irreversible
 146 dilation $\bar{w}_d = \int_0^t \dot{\gamma} \tan \psi(\kappa) \dot{d}_s dt$ accumulated during the loading history, we
 147 generalize the non inter-penetrability condition to

$$(d_n - w_d) \geq 0 \quad F_1(t'_n) \leq 0 \quad (d_n - w_d)F_1(t'_n) = 0 \quad (9)$$

148 2.3. Initial and boundary conditions

149 We assume that the elastic medium is initially in static equilibrium under
 150 a initial stress field σ_{ij}^o resulting in traction t_i^o on Γ . We assume that
 151 the initial state is such that the yielding criterion is not violated in any
 152 potential displacement discontinuity segments. Localized inelastic deformations
 153 therefore occurs as a result of either external loading (via an history
 154 of applied loads or displacements) or via internal pore fluid pressurization p
 155 which modifies the effective traction on the potential failure segments. We
 156 assume here the pore-pressure history known and uncoupled to mechanical
 157 deformation. Such time-dependent boundary conditions can be summarized
 158 as (in the local frame $i = s$, of the boundary):

$$t'_i(\mathbf{x}, t) = t_i^g(\mathbf{x}, t) - p(\mathbf{x}, t) \quad \text{on} \quad \Gamma_{t'_i} \quad (10)$$

159

$$u_i(\mathbf{x}, t) = u_i^g(\mathbf{x}, t) \quad \text{on} \quad \Gamma_{u_i} \quad (11)$$

160 with the usual conditions $\Gamma = \Gamma_{u_i} \cup \Gamma_{t'_i}$, and $\Gamma_{u_i} \cap \Gamma_{t'_i} = \emptyset$. $t_i^g(\mathbf{x}, t)$, $u_i^g(\mathbf{x}, t)$ and
 161 p denotes given applied traction vector, displacement components and fluid
 162 pore pressure respectively. Note that in the absence of fluid, the pressure p
 163 is null and t'_i reduces to t_i .

164 3. Numerical scheme

165 3.1. Boundary element method for elasto-static using a hierarchical matrix 166 approximation

167 We use the displacement discontinuity method [25] to discretize the elas-
 168 ticity equations (2). Upon discretization of Γ (union of all possible failing
 169 segments) into n_{segm} straight segments such that

$$\Gamma \approx \bigcup_{s=1}^{n_{segm}} \Gamma_s, \quad (12)$$

170 We assume that displacement discontinuities d_i vary linearly within an ele-
171 ment but discontinuously between adjacent elements (piece-wise linear ele-
172 ment). This assumption sets a weaker requirement at each intersecting mesh
173 node $n_{node} = n_{segm} + 1$ (i.e. no continuity of displacement discontinuities),
174 which notably allows to treat configurations of fractures intersection more
175 easily. For n_{segm} straight finite segments, we thus have $n = 4n_{segm}$ nodal dis-
176 placement discontinuities unknowns. By introducing this discretization into
177 the boundary integral elasticity equations (2), using a collocation method,
178 one finally obtain a $4n_{segm} \times 4n_{segm}$ linear system of equations

$$\mathbf{t} = \mathbf{t}^o + \mathbf{E}\mathbf{d}, \quad (13)$$

179 where \mathbf{t} and \mathbf{t}^o are respectively the current and far-field traction vectors, \mathbf{E}
180 is the fully populated elastic influence matrix and \mathbf{d} is the vector of nodal
181 displacement discontinuities. Because of the singular nature of equation (2),
182 collocation is performed at points located inside the displacement disconti-
183 nuity element - see [32] for discussion on their optimal location within the
184 reference straight element.

185 Due to the non-locality of the elasticity kernel, the elasticity matrix \mathbf{E}
186 is fully populated although diagonal dominant. The memory requirement to
187 store such a square matrix thus scales as $\mathcal{O}(n^2)$, setting a strict constraint
188 for current available laptops with 64-bit processors. Furthermore, the com-
189 putational complexity to solve the system of equations (13) with an iterative
190 method is $\mathcal{O}(k \cdot n^2)$ (where k is the number of iterations to reach convergence
191 in the iterative solver, with possibly $k \ll n$ if the system is well-conditioned).
192 In order to overcome these limits, we use a hierarchical matrix (\mathcal{H} -matrix)
193 representation of the BEM matrix combined with adaptive cross approxi-
194 mation to perform low-rank approximations [33]. This purely algebraic ac-
195 celeration technique makes use of the spatial decay of the elastic kernel to
196 approximate its far-field contributions via a data-sparse representation (low
197 rank approximation). This allows to reduce memory requirements and, at
198 the same time, speed up algebraic operations [34, 35]. First, a geometri-
199 cal binary tree $\mathcal{T}_{\mathcal{I}}$ associated with the location of the collocation points is
200 built. Its maximum depth is governed by a scalar parameter n_{leaf} that de-
201 fines the minimum cardinality of each cluster. Upon recursive evaluation of
202 the following admissibility condition

$$Adm(p, q) = \text{true} \iff \min\{\text{diam}(p), \text{diam}(q)\} \leq \eta \cdot \text{dist}(p, q), \quad (14)$$

203 to all the pair-nodes composing the block cluster tree $\mathcal{T}_{\mathcal{I}}$, a partitioning of the
 204 elastic matrix into admissible (*far-field*) and inadmissible (*near-field*) blocks
 205 is obtained. The diameter of a generic cluster $p \in \mathcal{T}_{\mathcal{I}}$ is defined as

$$\text{diam}(p) := \max_{i,j \in p} \|x_i - x_j\| \quad (15)$$

206 and the distance between two clusters $p, q \in \mathcal{T}_{\mathcal{I}}$ is

$$\text{dist}(p, q) := \min_{i \in p, j \in q} \|x_i - x_j\|. \quad (16)$$

207 The admissible blocks are approximated via low-rank matrices obtained with
 208 an adaptive cross approximation technique (see [34, 35, 36] for full details).
 209 Non-admissible blocks are stored and treated as dense matrices (full rank rep-
 210 resentation). It can be proved that by replacing the full elasticity matrix \mathbf{E}
 211 with its hierarchical approximation $\mathbf{E}_{\mathcal{H}}$, the generic computational complex-
 212 ity reduces to [35] $\mathcal{O}(n \times \log(n))$ for storage requirements and matrix-vector
 213 multiplications.

214 The construction of the \mathcal{H} -matrix representation of the initial matrix
 215 depends on 3 parameters: i) $\eta \geq 0$ governs the severity of the clustering (i.e.
 216 large value of η promote a more aggressive block partitioning, while $\eta = 0$
 217 results in no partitioning, i.e. $\mathbf{E}_{\mathcal{H}} = \mathbf{E}$), ii) $n_{leaf} > 0$ defines the maximum
 218 depth of the block cluster tree $\mathcal{T}_{\mathcal{I}}$ and iii) ϵ_{ACA} governs the accuracy of the
 219 low-rank approximation obtained via an adaptive cross approximation (see
 220 [34] for details for scalar problems and [36] for vector problems). The gain
 221 in memory storage with respect to the initial dense matrix is quantified by
 222 the memory compression ratio c_r given by

$$c_r(E_{\mathcal{H}}) = \frac{1}{n^2} \left(\sum_{(p,q) \in \text{Adm.}} \text{rank} \cdot (|p| + |q|) + \sum_{(p,q) \in \text{Non-Adm.}} |p| \cdot |q| \right) \quad (17)$$

223 while the accuracy of $\mathbf{E}_{\mathcal{H}}$ is function of η , n_{leaf} and ϵ_{ACA} . In the remaining,
 224 we consider only a hierarchical approximation $\mathbf{E}_{\mathcal{H}}$ of the elasticity matrix.

225 3.2. An implicit time-stepping scheme

226 For a given load / pore pressure history, the solution of the problem
 227 consists in the solution of the discretized elasto-static balance of momentum
 228 in combination with the set of inequalities constraints introduced in section
 229 2.2. Besides the inequalities, softening reinforces the non-linearity of the

230 problem. We use an implicit time-stepping scheme to obtain the solution at
 231 $t^{n+1} = t^n + \Delta t$ from a known solution at t^n . We solve for both the evolution
 232 of the displacement discontinuities as well as the corresponding tractions over
 233 the whole discretized mesh Γ . We use the notation $X^{n+1} = X^n + \Delta X$ to
 234 represent a generic time and space dependent variable $X(x, t)$ at time t^{n+1} .
 235 Over a time-step, the algorithm consists of two nested loops. The outer loop
 236 tracks the set of elements satisfying the yielding constraints and non inter-
 237 penetrability condition. The inner loop - for a given trial set of constraints
 238 - solves for the balance of momentum, and enforces the different equality
 239 constraints. Softening renders such an inner loop non-linear and we thus use
 240 a fixed-point scheme for its solution.

241 *3.2.1. Outer yielding loop*

242 The outer iterative loop is used to converge on the different inequalities
 243 constraints (yielding and non inter-penetrability conditions) for all the ele-
 244 ments within the mesh. At each iteration, the algorithm must identify the
 245 set of elements $\mathcal{S}_{a,1}$ active in tensile failure (satisfying eq. (3a)), the set of ele-
 246 ments $\mathcal{S}_{a,2}$ active in shear failure (satisfying eq. (3b)), and the set of elements
 247 $\mathcal{S}_{interp.}$ violating the inter-penetrability constraint eq. (9). The set of inactive
 248 elements (neither yield or interpenetrating) $\mathcal{S}_{inact.}$ is just the complement

$$249 \quad \mathcal{S}_{inact.} \notin \{\mathcal{S}_{a,I} \cup \mathcal{S}_{a,II} \cup \mathcal{S}_{interp.}\}$$

250 such that the union of all these sets equals the total number of elements in
 251 the mesh. A priori, these sets are unknown. Over a load/time step, during
 252 this iterative procedure, an element can thus switch from being inactive (not
 253 violating either the yield or contact conditions) to being active - where then
 254 the yield constraints are enforced (similarly for contact). For each set of
 255 segments, different constraints have to be enforced in combination with equi-
 256 librium, either in terms of traction or in terms of displacement discontinuity
 257 (as discussed in section 2.2).

258 The convergence of this outer loop is achieved when these different sets
 259 remain identical between two subsequent iterations, meaning that all the
 260 inequality constraints are satisfied.

261 *3.2.2. Solution of the equilibrium under constraints*

262 For a given set of constraints assigned to different elements, we solve for
 263 the balance of momentum combined with the corresponding prescribed set

264 of equality constraints. First, we rewrite the equilibrium in terms of effective
 265 traction, such that the discretized elasticity equations (13) becomes

$$\mathbf{t}^{\prime,n+1} = \mathbf{t}^o + \mathbf{E}_{\mathcal{H}} \mathbf{d}^{n+1} - \mathbf{p}_{coll}^{n+1}, \quad (18)$$

266 where $\mathbf{p}_{coll}^{n+1} = (0, p_1, 0, \dots, 0, p_i, \dots)$ is a vector containing the current pore
 267 pressure vector evaluated at the different collocation points, which acts only
 268 on the normal traction component.

269 In addition to these $4n_{elts}$ equations, we prescribe $4n_{elts}$ equations in
 270 relations to the type of constraint acting on each element. This results in a
 271 $8n_{elts} \times 8n_{elts}$ linear system with both the displacement discontinuities and
 272 the effective tractions as unknowns.

273 We now list the different constraints assigned to the different set of ele-
 274 ments.

275 **Set of elements active in tensile failure $\mathcal{S}_{a,1}$:** Pure tensile failure
 276 is active in an element when $F_1(t_n^{\prime,n+1}) > 0$ and $h(t_s^{n+1}, t_n^{\prime,n+1}) < 0$ at both
 277 collocation points. We thus enforce eq. (7b), and the discretized equations
 278 for one collocation point of an active tensile element are

$$t_n^{\prime,n+1} = -\sigma_c(\kappa^{n+1}, \kappa_m^{n+1}), \quad \Delta d_s = 0, \quad (19)$$

279 which can be rewritten in matrix form as

$$\begin{bmatrix} 0 & 0 \\ 0 & 1 \end{bmatrix} \begin{bmatrix} t_s^{n+1} \\ t_n^{\prime,n+1} \end{bmatrix} = \begin{bmatrix} 0 \\ -\sigma_c(\kappa^{n+1}, \kappa_m^{n+1}) \end{bmatrix}, \quad \begin{bmatrix} 1 & 0 \\ 0 & 0 \end{bmatrix} \begin{bmatrix} \Delta d_s \\ \Delta d_n \end{bmatrix} = \begin{bmatrix} 0 \\ 0 \end{bmatrix} \quad (20)$$

280 **Set of elements active in shear failure $\mathcal{S}_{a,2}$.** Similarly, an element for
 281 which $F_2(t_s^{n+1}, t_n^{\prime,n+1}) > 0$ & $h(t_s^{n+1}, t_n^{\prime,n+1}) \geq 0$ at both collocation points,
 282 we must enforce $F_2 = 0$ and the dilatant flow rule (5b). For one collocation
 283 point of an active shear segment, we have

$$\begin{aligned} t_s^{n+1} &= c(\kappa^{n+1}, \kappa_m^{n+1}) + f(|d_s^{n+1}|, \delta_m^{n+1}) t_n^{\prime,n+1}, \\ \Delta d_n &= |\Delta d_s| \text{sign}(t_s) \tan(\psi(|d_s^{n+1}|, \delta_m^{n+1})), \end{aligned} \quad (21)$$

284 which can be rewritten in matrix form as

$$\begin{bmatrix} 1 & -f(|d_s^{n+1}|, \delta_m^{n+1}) \\ 0 & 0 \end{bmatrix} \begin{bmatrix} t_s^{n+1} \\ t_n^{\prime,n+1} \end{bmatrix} = \begin{bmatrix} c(\kappa^{n+1}, \kappa_m^{n+1}) \\ 0 \end{bmatrix}, \quad (22)$$

$$\begin{bmatrix} 0 & 0 \\ -\text{sign}(t_s) \tan(\psi(|d_s^{n+1}|, \delta_m^{n+1})) & 1 \end{bmatrix} \begin{bmatrix} \Delta d_s \\ \Delta d_n \end{bmatrix} = \begin{bmatrix} 0 \\ 0 \end{bmatrix}$$

285 **Inter-penetrating segments** \mathcal{S}_{interp} . if the normal displacement discontinuity on one mesh node is lower than the minimum admissible value \bar{w}_d ,
 286 then we enforce
 287

$$288 \quad d_n^{n+1} = \bar{w}_d \quad \Delta d_s = 0,$$

289 which in incremental and matrix form reads

$$\begin{bmatrix} 1 & 0 \\ 0 & 1 \end{bmatrix} \begin{bmatrix} \Delta d_s \\ \Delta d_n \end{bmatrix} = \begin{bmatrix} 0 \\ \bar{w}_m - d_n^n \end{bmatrix} \quad (23)$$

290 **Inactive elements** \mathcal{S}_{inact} . are neither at failure or violate the inter-penetrability
 291 constraint. The rate of displacement discontinuities is zero and we enforce

$$\begin{bmatrix} 1 & 0 \\ 0 & 1 \end{bmatrix} \begin{bmatrix} \Delta d_s \\ \Delta d_n \end{bmatrix} = \begin{bmatrix} 0 \\ 0 \end{bmatrix} \quad (24)$$

292 *3.2.3. Solution of the tangent system for the trial active sets*

293 By considering all the nodes and collocation points of a computational
 294 mesh, these different constraints depending on the active set of constraints
 295 provide a set of $4n_{segm}$ equations in addition to the elasto-static balance of
 296 momentum. We obtain the following system of $8n_{segm} \times 8n_{segm}$ equations

$$\underbrace{\begin{bmatrix} \mathbf{E}_{\mathcal{H}} & \mathbf{I} \\ \mathbf{B} & \mathbf{C} \end{bmatrix}}_{\mathbf{A}} \underbrace{\begin{bmatrix} \Delta \mathbf{d} \\ \mathbf{t}^{l,n+1} \end{bmatrix}}_{\mathbf{x}} = \underbrace{\begin{bmatrix} \mathbf{t}^o + \mathbf{E}_{\mathcal{H}} \mathbf{d}^n - \mathbf{p}_{coll}^{n+1} \\ \mathbf{a} \end{bmatrix}}_{\mathbf{y}} \quad (25)$$

297 for the unknowns increment of displacement discontinuities $\Delta \mathbf{d}$ and current
 298 effective tractions $\mathbf{t}^{l,n+1}$. In the system of equations (25), \mathbf{I} is a $4n_{segm} \times 4n_{segm}$
 299 identity matrix, \mathbf{a} is a $4n_{segm} \times 1$ vector that contains the right hand sides
 300 of the different equality constraints previously described. The matrix \mathbf{B} and
 301 \mathbf{C} are sparse and contain the constraints in term of displacement discontinuities and effective traction respectively, given by the constitutive interface
 302 relations. The pattern of these block matrices depends on the different set
 303 of constraints and thus may differ between iterations of the yielding loop.
 304

305 The system of equations (25) is non-linear when the material's strength
 306 parameters soften with current plastic deformations. For this reason, we
 307 adopt a fixed point iterative scheme combined with under-relaxation [37].
 308 Iterations are ended when subsequent estimates of both increment of displacement discontinuities and effective traction fall within a given relative
 309

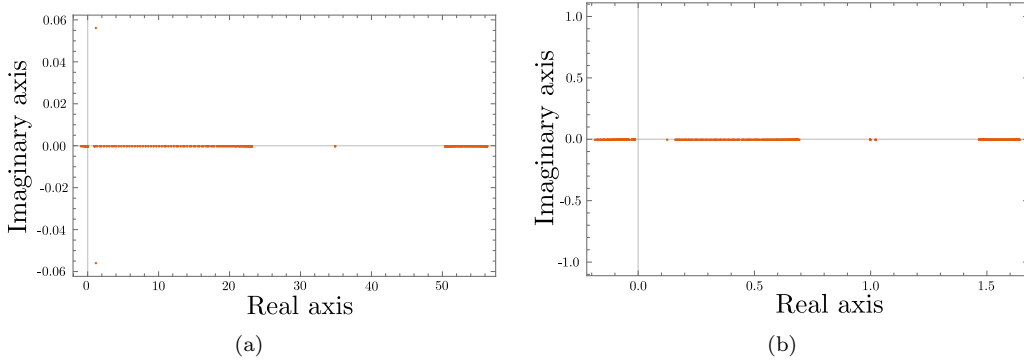


Figure 3: Examples of eigenvalues distribution along the complex plane for the matrix \mathbf{A} that arises from final system of equations (25) prior (a) and after (b) application of preconditioning matrix \mathbf{P}_{up} . Case of a planar fracture in an infinite domain discretized with 100 equal-sized segments with six element active in shear. The spectral radius of the original matrix \mathbf{A} is $\rho(\mathbf{A}) \simeq 56.3$, while the one of the preconditioned matrix is $\rho(\mathbf{A}_p) \simeq 1.64$.

310 tolerance ϵ_{tol} . At a given iteration of the fixed point scheme, the solution of
 311 the system (25) is obtained via a Krylov sub-space iterative method, specif-
 312 ically the generalized minimal residual method (GMRES).

313 Although the sub-blocks \mathbf{B} and \mathbf{C} are singular sparse matrices, \mathbf{A} has
 314 always full rank. Furthermore, although the final matrix \mathbf{A} is sparse, it is not
 315 diagonal dominant and highly non-symmetric. Figure 3a displays an example
 316 of spectral properties of matrix \mathbf{A} arising from the example of a a planar
 317 fracture embedded in an infinite medium discretized with 100 equal-sized
 318 elements, with 6 of them belonging to $\mathcal{S}_{a,2}$, while the others being inactive.
 319 The eigenvalues of \mathbf{A} are spread over a wide range on the complex plane, both
 320 along the real and the imaginary axis (Figure 3a). The spectral radius for
 321 such an example is indeed $\rho(\mathbf{A}) = 56.3$, resulting in a slow convergence during
 322 GMRES iterations. In order to improve the spectral properties of matrix \mathbf{A} ,
 323 we develop a block preconditioner approach. Unlike preconditioners based
 324 on algebraic techniques that require little knowledge of the problem under
 325 investigation [38], the preconditioning of system (25) is tailored to the pattern
 326 of matrix of coefficient \mathbf{A} . Starting from the observation that if the sub-
 327 block \mathbf{C} is null, which is the case when all the mesh elements are inactive,
 328 the pattern of the resulting system of equations is equivalent to the one that
 329 arises from non-symmetric saddle point problems, we adapt a preconditioner
 330 that is tailored for such class of problems (see [38, 39, 40, 41] for such type

331 of pre-conditioners). Following [38], we introduce an upper-triangular block
 332 preconditioner matrix on the right side of system (25) such that the latter
 333 can be rewritten as

$$\mathbf{A}\mathbf{P}_{up}^{-1}\mathbf{u} = \mathbf{y}, \quad \mathbf{u} = \mathbf{P}_{up}\mathbf{x}, \quad (26)$$

334 where the preconditioning matrix \mathbf{P}_{up} reads

$$\mathbf{P}_{up} = \begin{bmatrix} \mathbf{D}_{\mathbf{E}_{\mathcal{H}}} & \mathbf{I} \\ \mathbf{0} & \mathbf{S} \end{bmatrix} \quad (27)$$

335 and its inverse is given by

$$\mathbf{P}_{up}^{-1} = \begin{bmatrix} \mathbf{D}_{\mathbf{E}_{\mathcal{H}}}^{-1} & -\mathbf{D}_{\mathbf{E}_{\mathcal{H}}}^{-1}\mathbf{S}^{-1} \\ \mathbf{0} & \mathbf{S}^{-1} \end{bmatrix} \quad (28)$$

336 In equation (27) and (28), $\mathbf{D}_{\mathbf{E}_{\mathcal{H}}}$ is the diagonal of the hierarchical elasticity
 337 matrix $\mathbf{E}_{\mathcal{H}}$ and $\mathbf{S} = \mathbf{C} - \mathbf{B}\mathbf{D}_{\mathbf{E}_{\mathcal{H}}}^{-1}$ is the Schur complement with respect to
 338 $\mathbf{D}_{\mathbf{E}_{\mathcal{H}}}$. Note that if $\mathbf{D}_{\mathbf{E}_{\mathcal{H}}} = \mathbf{E}_{\mathcal{H}}$, then the spectrum of $\mathbf{A}\mathbf{P}_{up}^{-1}$ is $\rho(\mathbf{A}\mathbf{P}_{up}^{-1}) = \{1\}$
 339 such that an iterative method like GMRES would converge in at most two
 340 iterations [38]. In practice, however, we do not want to compute the inverse
 341 of the hierarchical elasticity matrix. We consider only the inverse of the
 342 diagonal self-effect elastic contributions. It is worth mentioning that for
 343 nonsymmetric saddle point problems, this choice is commonly taken when
 344 the sub-block (1,1) is diagonal dominant, for which it is proved that a good
 345 clustering of the eigenvalues around 1, $\frac{1}{2}(1 + \sqrt{5})$ and $\frac{1}{2}(1 - \sqrt{5})$ is obtained
 346 [38, 39] (although it does not prevent the preconditioned matrix from having
 347 its eigenvalues on both side of the imaginary axis). Upon application of the
 348 right upper-triangular preconditioner \mathbf{P}_{up}^{-1} , the system of equations (26) can
 349 be re-written as the following two systems:

$$\underbrace{\begin{bmatrix} \mathbf{E}_{\mathcal{H}}\mathbf{D}_{\mathbf{E}_{\mathcal{H}}}^{-1} & -\mathbf{E}_{\mathcal{H}}\mathbf{D}_{\mathbf{E}_{\mathcal{H}}}^{-1}\mathbf{S}^{-1} + \mathbf{S}^{-1} \\ \mathbf{B}\mathbf{D}_{\mathbf{E}_{\mathcal{H}}}^{-1} & -\mathbf{B}\mathbf{D}_{\mathbf{E}_{\mathcal{H}}}^{-1}\mathbf{S}^{-1} + \mathbf{C}\mathbf{S}^{-1} \end{bmatrix}}_1 \begin{bmatrix} \mathbf{u}_1 \\ \mathbf{u}_2 \end{bmatrix} = \begin{bmatrix} \mathbf{y}_1 \\ \mathbf{y}_2 \end{bmatrix}, \quad \underbrace{\begin{bmatrix} \mathbf{D}_{\mathbf{E}_{\mathcal{H}}} & \mathbf{I} \\ \mathbf{0} & \mathbf{S} \end{bmatrix}}_2 \begin{bmatrix} \mathbf{x}_1 \\ \mathbf{x}_2 \end{bmatrix} = \begin{bmatrix} \mathbf{u}_1 \\ \mathbf{u}_2 \end{bmatrix} \quad (29)$$

350 As one can notice, the exact inverse of the Schur complement is needed
 351 for numerical resolution of system 1. Although the Schur complement is a
 352 sparse matrix and fast algorithms have been developed to obtain its inverse
 353 (see [42, 43] for examples), its inverse is typically not sparse. For large scale
 354 problems, therefore, this operation would costly memory-wise. In order to

355 avoid computing the inverse of the Schur complement \mathbf{S} , we perform a change
 356 of variable

$$357 \quad \mathbf{z}_2 = \mathbf{S}^{-1}\mathbf{u}_2$$

358 such that the system 1 of equation (29) reduces to

$$\underbrace{\begin{bmatrix} \mathbf{E}_{\mathcal{H}}\mathbf{D}_{\mathbf{E}_{\mathcal{H}}}^{-1} & -\mathbf{E}_{\mathcal{H}}\mathbf{D}_{\mathbf{E}_{\mathcal{H}}}^{-1} + \mathbf{I} \\ \mathbf{B}\mathbf{D}_{\mathbf{E}_{\mathcal{H}}}^{-1} & -\mathbf{B}\mathbf{D}_{\mathbf{E}_{\mathcal{H}}}^{-1} + \mathbf{C} \end{bmatrix}}_{\mathbf{A}_p} \begin{bmatrix} \mathbf{u}_1 \\ \mathbf{z}_2 \end{bmatrix} = \begin{bmatrix} \mathbf{y}_1 \\ \mathbf{y}_2 \end{bmatrix}, \quad (30)$$

359 where \mathbf{A}_p denotes the preconditioned matrix of coefficients. Note that, since
 360 the Schur complement and its inverse are ultimately discarded, system (30)
 361 can be found in a more direct way by directly setting $\mathbf{x} = \mathbf{P}^{-1}\mathbf{z}$ in (25), with
 362 $\mathbf{z} = \begin{bmatrix} \mathbf{u}_1 \\ \mathbf{z}_2 \end{bmatrix}$ and the preconditioning matrix $\mathbf{P} = \begin{bmatrix} \mathbf{D}_{\mathbf{E}_{\mathcal{H}}} & \mathbf{I} \\ \mathbf{0} & \mathbf{I} \end{bmatrix}$.

363 In order to highlight the effect of the preconditioner \mathbf{P}_{up} , we show in
 364 Figure 3b the spectral properties of the preconditioned matrix \mathbf{A}_p that arises
 365 from the same example previously described. The improvement is clear. The
 366 eigenvalues of the pre-conditioned matrix are spread over a much more narrow
 367 range (see Figure 3) and more importantly all the eigenvalues are real. The
 368 spectral radius in this particular example is $\rho(\mathbf{A}_p) \sim 1.64$, roughly 3% of the
 369 one of the initial system \mathbf{A} . The preconditioned system of equations (30)
 370 is solved via GMRES iterative method for the unknown vectors \mathbf{u}_1 and \mathbf{z}_2 .
 371 Once the iterative solution converges within a given tolerance, the solution
 372 of the preconditioned mechanical problem (26) can be simply obtained by
 373 performing the proper matrix-vector multiplications, i.e.

$$\mathbf{t}',n+1 = \mathbf{x}_2 = \mathbf{z}_2, \quad \Delta\mathbf{d} = \mathbf{x}_1 = \mathbf{D}_{\mathbf{E}_{\mathcal{H}}}^{-1}(\mathbf{u}_1 - \mathbf{z}_2) \quad (31)$$

374 Note that the numerical solution of the preconditioned system (26) via a
 375 GMRES iterative scheme does never involve any matrix inversions, but only
 376 matrix-vector products.

377 The non-linear mechanical problem (25) converges when the relative dif-
 378 ference between two subsequent estimates of both increment of displacement
 379 discontinuities and effective tractions fall below a given tolerance (typically
 380 $10^{-6} - 10^{-8}$). The algorithm then moves back to the yielding loop to recheck
 381 the inequalities constraints.

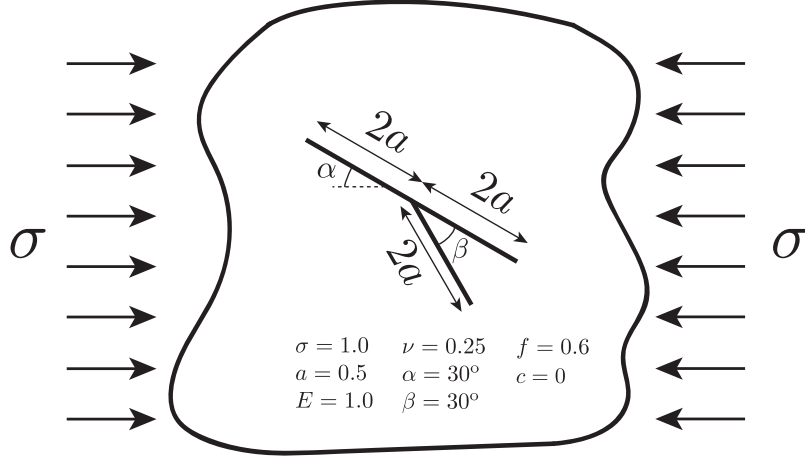


Figure 4: Sketch of branched frictional fault system subjected to a remote compressive load. All the material and geometrical parameters are reported in the figure.

382 4. Illustrative examples

383 4.1. A branched frictional fault system

384 As first example, we present the case of a branched frictional fault system
 385 embedded in an infinite domain and subjected to a remote static compressive
 386 load (see Figure 4 in which all material and geometrical parameters are re-
 387 ported). The remote load translates into applied tractions along the branched
 388 fault that are such to overcome its frictional strength and hence activate a
 389 shear crack in both branches of the system due to elastic interactions. In
 390 this example, the frictional properties are constant (no softening), cohesion
 391 as well as shear-induced dilatancy are neglected ($c = 0$, $\tan \psi_p = 0$).

392 No analytical solution exists for this problem. We thus compare our
 393 results with previously reported numerical results for this same problem - see
 394 Maerten et al. [44] who also compare their solutions with the one of Cooke and
 395 Pollard [45]. We discretize the branched fault system with $2 \cdot 10^4$ equal-sized
 396 straight segments (notably $1.2 \cdot 10^4$ elements for the main branch of length
 397 $4a$ and $0.8 \cdot 10^4$ segments for the secondary branch of length $2a$) for a total
 398 of $1.6 \cdot 10^5$ degrees of freedom (tractions and displacement discontinuities).
 399 Using $\eta = 3$, $\epsilon_{ACA} = 10^{-6}$, and $n_{leaf} = 300$, we obtain a compression ratio
 400 of $c_r(\mathbf{E}_{\mathcal{H}}) = 0.025$ for the hierarchical matrix representation of the elastic
 401 system. This allows to solve this problem on laptop using less than 3GB of

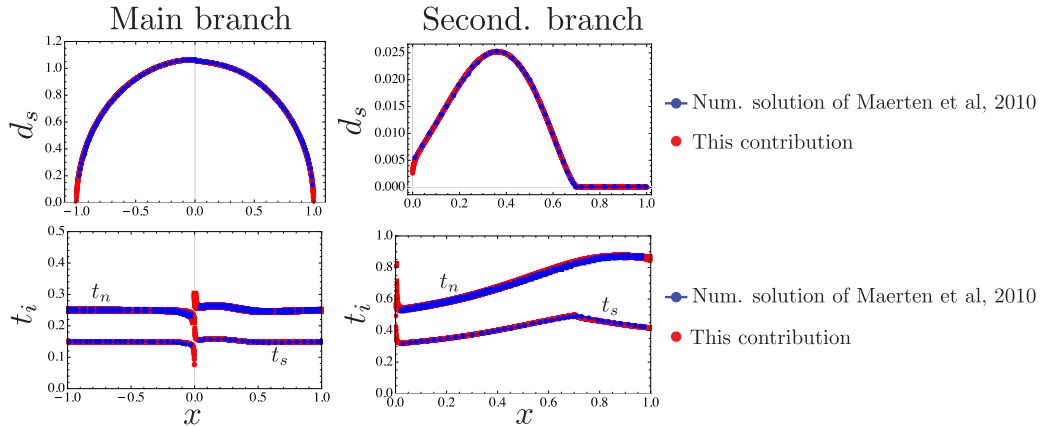


Figure 5: Comparison between the numerical results obtained with the developed solver and the ones of Maerten et al. [44] in terms of slip and tractions distribution along the main fault branch (left panel) of length $4a$ and along the secondary branch of length $2a$ (right panel).

402 RAM. It would have been impossible using the fully populated elastic matrix
 403 which requires $\sim 51\text{GB}$ of memory storage in double precision.

404 The comparison of our numerical results with the one reported by Maerten
 405 et al. [44] are displayed in Figure 5. A good match between our numerical
 406 results and the ones of Maerten et al. [44] is obtained, both in terms of
 407 slip and tractions distributions. The position of the shear crack tip on the
 408 secondary branch is accurately captured, denoting thus that the algorithm
 409 devised works correctly for the frictional deformation.

410 4.2. Tensile wellbore failure

411 We now switch to an example associated with pure tensile failure and
 412 mode I cohesive crack initiation and growth from a wellbore located in a
 413 infinite domain (see Figure 6). We consider the case of an increase of the
 414 wellbore pressure, while the far-field in-situ stress remains constant. The
 415 material properties (large cohesion, finite tensile strength) as well as the
 416 in-situ stress field are taken to favor pure tensile failure. Upon increase
 417 of the wellbore pressure ($t_n(r = R) = p_b(t)$, $t_s(r = R) = 0$), a tensile
 418 fracture initiates and propagates symmetrically with respect to the centre
 419 of the wellbore along the direction of the maximum principal in-situ stress
 420 (here σ_{xx}). The "Kirsch" elastic solution [46] allows to estimate the wellbore
 421 pressure $p_{b,\text{strength}} = \sigma_c - \sigma_{xx} + 3\sigma_{yy}$ at which the hoop stress $\sigma_{\theta\theta}$ around the

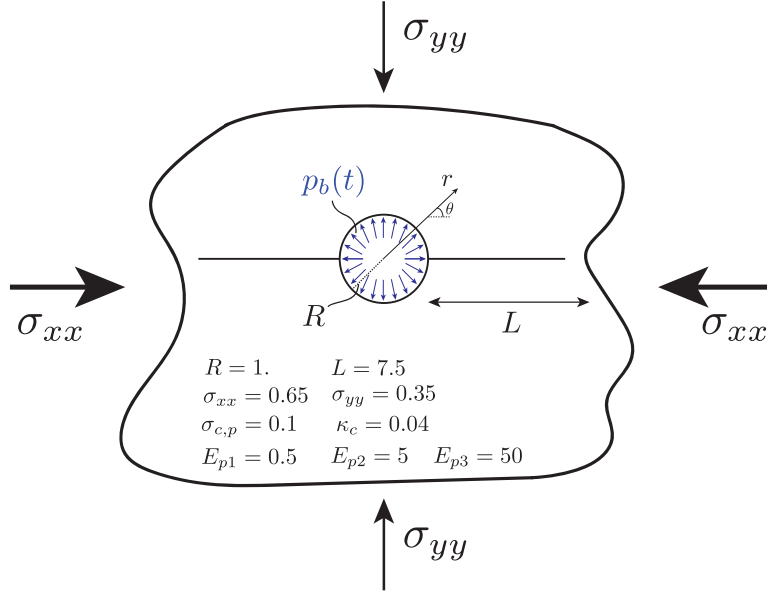


Figure 6: Sketch of plane strain pressurized wellbore & far field loading conditions. The elasticity matrix is compressed using: $\eta = 3$, $\epsilon_{ACA} = 10^{-6}$, $n_{leaf} = 32$ resulting in a compression ratio $c_r = 0.1132$. We use a small value of n_{leaf} here as the problem is rather small (924 elements / 3712 displacement discontinuity unknowns).

422 wellbore reaches the material tensile strength σ_c as well as its location (here
423 at $\theta = 0$ for the given deviatoric far-field stress and $p_{b,\text{strength}} = 0.5$ for the
424 parameters of Figure 6). Due to the softening of the tensile strength, this
425 problem exhibit a size effect on the pressure and corresponding crack length
426 at which the crack completely nucleates. Specifically, the crack initiation
427 pressure of the borehole is defined as the borehole pressure at which all
428 the fracture energy has been released (or similarly at which the opening
429 at the borehole wall equals the critical opening κ_c at which cohesive forces
430 vanishes). This initiation pressure is larger than $p_{b,\text{strength}}$ predicted from a
431 strength criteria [47, 48]. The size effect is governed by the Irwin number
432 defined as the ratio \mathcal{I} between the material length scale $l_m = \frac{G_c E_p}{\sigma_c^2}$ (with
433 $G_c = \frac{\sigma_{c,p} \kappa_c}{2}$ the critical fracture energy) and the structural length scale -
434 here the wellbore radius $l_s = R$. For that particular configuration large
435 values of \mathcal{I} corresponds to cases where fracture energy requirement govern
436 crack nucleation, while strength dominated failure for low value of \mathcal{I} .

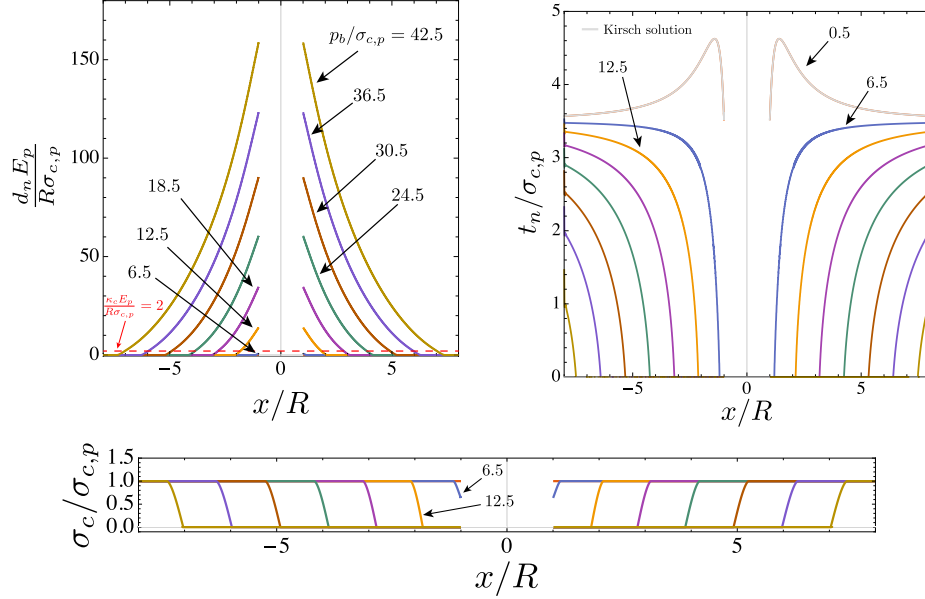


Figure 7: Spatial profiles of normalized opening displacement discontinuity $\frac{d_n E_p}{R \sigma_{c,p}}$ (top-left), normal traction $t_n/\sigma_{c,p}$ (top-right) and tensile strength $\sigma_c/\sigma_{c,p}$ (bottom) along the horizontal direction (i.e. $\theta = 0$), at different normalized wellbore pressure $p_b/\sigma_{c,p}$ - $\mathcal{I}_2 = 1$ case. The light grey lines represent the Kirsch analytical solution valid in the elastic range (prior to crack nucleation).

437 We perform three different simulations, varying the plane strain Young
 438 modulus E_p to cover three distinct values of the Irwin number ($\mathcal{I}_1 = 0.1$, $\mathcal{I}_2 =$
 439 1 and $\mathcal{I}_3 = 10$) while keeping the other parameters constant (see Figure 6).
 440 In addition to the wellbore boundary, we mesh a potential horizontal line
 441 where the crack can nucleate with 924 equal-sized straight elements. Table
 442 1 compares our numerical results to the ones reported in Lecampion [47] for
 443 the scaled crack initiation pressure for different value of \mathcal{I} . The results are
 444 similar within 5% relative difference.

445 Figure 7 displays the spatial profile of normalized opening displacement
 446 discontinuities (top-left), normal traction (top-right) and normal traction
 447 t_n (bottom) along $\theta = 0$, for increasing values of the normalized borehole
 448 pressure $p_b/\sigma_{c,p}$. For low values of $p_b/\sigma_{c,p}$ ($p_b/\sigma_{c,p} < 5$ here), the response
 449 is elastic: the spatial profile of the normal traction matches perfectly the
 450 Kirsch elastic analytical solution (see the light grey line in Figure 7 top-right
 451 for $p_b/\sigma_{c,p} = 0.5$). When the borehole pressure reaches the value given by

452 the strength criterion (here $p_b/\sigma_{c,p} = 5$), a crack starts to propagate sym-
453 metrically, and reduction of the normal tractions associated with softening
454 can be observed in a cohesive zone near the crack tips (see Figure 7).

455 *4.3. Shear-banding in uniaxial compression*

456 The examples presented so far involved an infinite medium. However, the
457 numerical scheme devised allows to readily investigate problems with finite
458 domains whose boundary conditions are known a priori. Effective tractions
459 and/or displacement discontinuities (see equations (10-11)) can thus be easily
460 imposed through the matrices \mathbf{B} and \mathbf{C} in system (25). As a simple example,
461 a bounded domain with traction-free boundary conditions must satisfy $t'_i = 0$
462 all along its boundaries. These constraints are enforced directly in matrix \mathbf{C}
463 of system (25).

464 We discuss now the case of a rectangular bar under plane strain conditions
465 subjected to uni-axial compression (see Figure 8 for all geometrical and ma-
466 terial parameters).

467 Our aim is to illustrate how by introducing a number of segments where
468 localized deformation can possibly takes place, the final response of the mate-
469 rial is akin to the one obtained with a conventional elasto-plastic approach.
470 As a result, the mesh depicted in Figure 8 should not be confused with a
471 finite element mesh as we use a boundary element method to solve for the
472 balance of momentum. Indeed, the segments located inside the bar are solely
473 here to capture localized inelastic deformation. For value of the uniaxial load
474 below the yield stress, all the displacement discontinuities of the element in-
475 side the domain are zero and the elastic response is captured by the elements
476 discretized the material boundary. The yield properties of all segments are
477 taken to correspond to a purely cohesive material (zero friction and infinite
478 tensile strength) - which translates in a Tresca material globally. We first
479 investigate the case of perfect plasticity without softening, and then discuss
480 the effect of softening.

481 In absence of softening, the elasto-plastic response for such a configura-
482 tion yields homogeneous plastic deformation in the case of a "defect" free
483 homogeneous material. An elastic perfectly plastic solid with smooth yield
484 surface is indeed quite resistant to localization of deformation into a shear
485 band [49, 50]. However, small heterogeneities in strength typically results
486 in localization of deformation into shear bands. This is notably the case
487 when a "defect" is introduced in the middle of the bar - see [3, 51, 4, 52] for
488 discussion of the uni-axial tension case.

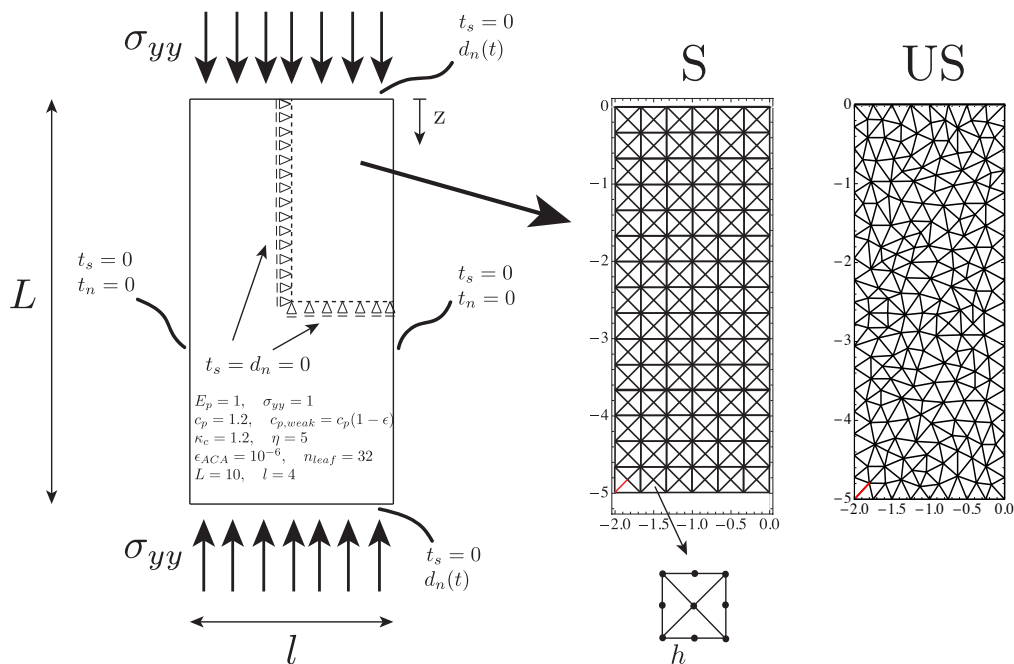


Figure 8: A rectangular bar subjected to uni-axial compression. Only one quarter of the bar is modelled due to symmetry. A set of structured (S) or unstructured (US) potential segments of failures are tested to investigate the corresponding mesh dependency. A defect (segment with lower strength) is introduced near the bottom-left corner (red segment).

489 In order to investigate the mesh dependency and the intrinsic limits/advantages
 490 of our method, we solve the problem using two computational boundary el-
 491 ement meshes (see Figure 8-right): i) a structured mesh (S), for which the
 492 potential failure segments for plasticity localization follow a specific geomet-
 493 rical pattern which includes the preferential 45° direction for a Tresca ma-
 494 terial, and ii) an un-structured mesh (US) whose potential failure segments
 495 are randomly oriented in the problem domain. We introduce a defect at
 496 the bottom-left corner of the bar by reducing the frictional strength of the
 497 extreme bottom-left segment such that (see red segment in Figure 8-right)

$$498 \quad c_{p,weak} = c_p(1 - \epsilon),$$

499 where ϵ is a dimensionless parameter that quantify the intensity of the defect.
 500 The uniform compression within the bar is increased by prescribing increasing
 501 the normal displacement discontinuities of the top surface.

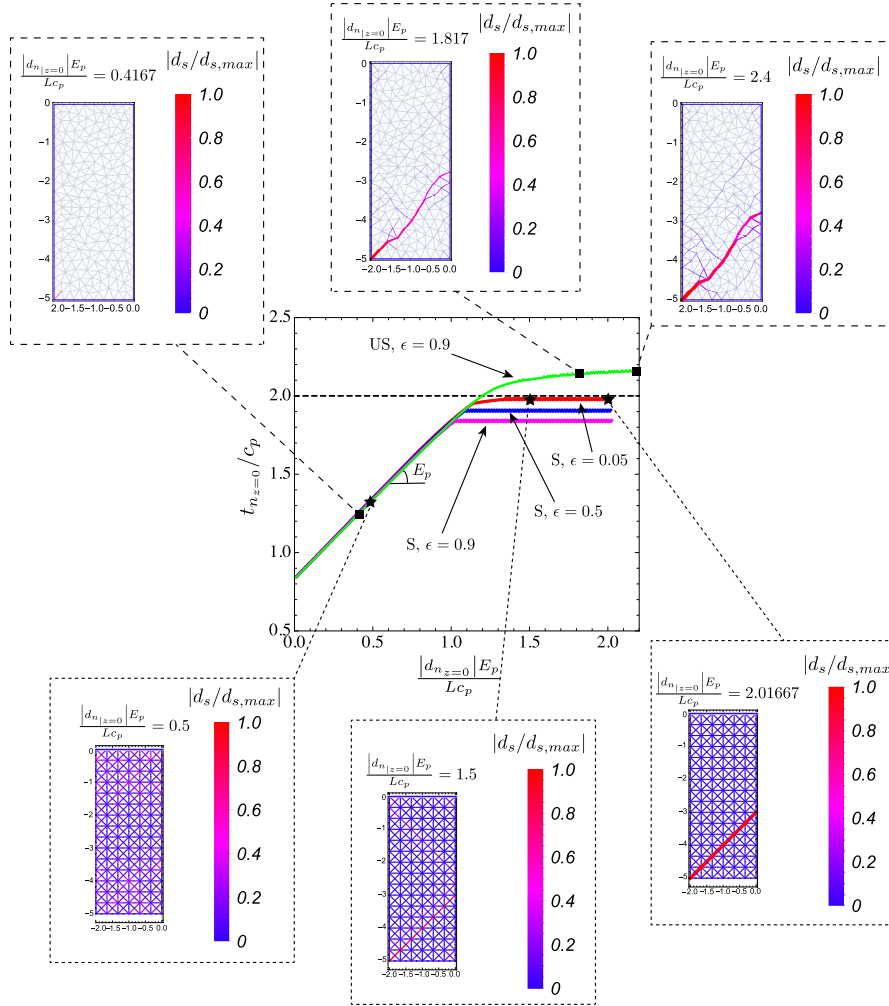


Figure 9: Load-displacement curves for both structured (S) and unstructured (US) mesh, for different intensity values of in-homogeneity ϵ (center plot). The horizontal dashed black line represents the (normalized) traction value at $z = 0$ for plasticity nucleation that one would get if an homogeneous bar with only a pre-meshed slip line at 45° is considered (from the bottom-left corner of the bar to the tractions free lateral side). Evolution of normalized plastic shear deformations $|d_s/d_{s,max}|$ along pre-existing potential failure segments (structured and unstructured mesh) is displayed at different moment along the stress-strain curve. The color and the thickness of each pre-existing segment is proportional to the corresponding shear displacement discontinuity accumulated.

502 The plot in the centre of Figure 9 displays the load-displacement curves
 503 for both structured (S) and unstructured (US) mesh for different intensity

504 values of in-homogeneity ϵ , without any softening of cohesion. Although the
 505 material response is qualitatively the same regardless the type of mesh and
 506 the intensity of the defect, the level of compression at which a shear band is
 507 nucleated is not mesh independent.

508 Referring to the case of structured mesh with $\epsilon = 0.05$, the load-displacement

509 (using the normalized displacement at the top of the bar $\frac{|d_{n|z=0}| E_p}{Lc_p}$) response

510 of the material for compression values lower than ~ 1.05 is perfectly linear-
 511 elastic. For increasing values of compression, shear plastic deformations first
 512 take place near the inhomogeneity, up to a given value of compression after
 513 which a main shear band is triggered, from the bottom-left corner to the
 514 right side of the bar with an inclination of 45° with respect to the minimum
 515 principal direction. At this specific value of compression, a small increase
 516 of compressive normal stress leads to a large increment of inelastic deforma-
 517 tions. Localized shearing along a favourably oriented plane occur and
 518 the intensity of slip accumulated increases significantly (see the snapshots

519 for $\frac{|d_{n|z=0}| E_p}{Lc_p} = 1.5/2.016$ in the bottom-right of Figure 9). Because of

520 the structured mesh adopted (that embeds the theoretical failure line of the
 521 shear band) and the low value of inhomogeneity used in this example, the
 522 nucleation of the shear band occurs at a compression value that is slightly
 523 below the theoretical value of $2c$ that one would get if an homogeneous bar
 524 with only a pre-meshed slip line at 45° is considered (see horizontal dashed
 525 black line in Figure 9-plot in the centre). This picture, however, changes for
 526 defects with larger intensities (i.e. larger ϵ) or when an unstructured mesh
 527 is used. In the former case, larger stress concentrations near the bottom-left
 528 corner of the bar promote the nucleation of a shear band at lower values of
 529 compressive stress (as expected - see plot in the centre of Figure 9), whereas
 530 the material response in the case of the unstructured mesh is clearly stiffer
 531 (compared to the one of the structured mesh, for the same value of inho-
 532 mogeneity - see the green curve in the centre plot of Figure 9), leading to a
 533 shear band nucleation at larger values of compression. This latter scenario is
 534 the result of a mesh dependency that kicks in when the pre-existing potential
 535 failure segments are not exactly aligned along the actual theoretical failure
 536 plane.

537 For specific problems that involve shear band localization along known

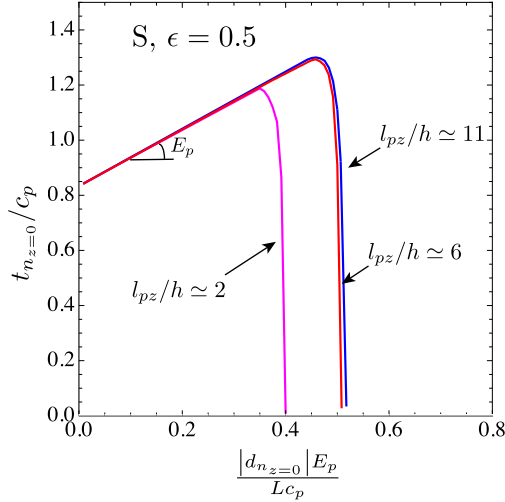


Figure 10: Softening case - Load-displacement curves for a bar subjected to uni-axial compression, discretized with a structured mesh (S) with an initial defect of intensity $\epsilon = 0.5$. Effect of the mesh size h as function with respect to the softening material length scale $l_{pz} = \frac{E_p \kappa_c}{c_p}$.

538 failure planes, the numerical solver introduced in section 3 is mesh independent
 539 dependent upon meshing the a-priori known failure plane(s) with potential fail-
 540 ing segments. More interestingly, the introduction of softening (which typi-
 541 cally strongly re-inforce mesh dependency when using bulk elasto-plasticity)
 542 does not alter this conclusion as long as the softening material length scale
 543 $l_{pz} = \frac{E_p \kappa_c}{c_p}$ is properly captured numerically. This is clearly seen in Figure
 544 10, where the load-displacement curve for the structured mesh with an in-
 545 homogeneity of $\epsilon = 0.5$ is reported for different ratio of l_{pz}/h being h the
 546 element size. For a number of elements within l_{pz} larger than ~ 5 , the load-
 547 displacement curves are similar both in the linear elastic and in the softening
 548 plastic range.

549 4.4. Active Earth pressure against a rigid retaining wall

As another example of interior problem, we present the case of a retaining wall under plain strain conditions, subjected to active Earth pressure (see sketch in Figure 11-top). We assume that the retaining wall is rigid and perfectly smooth (zero friction between the soil and the wall). We assume a

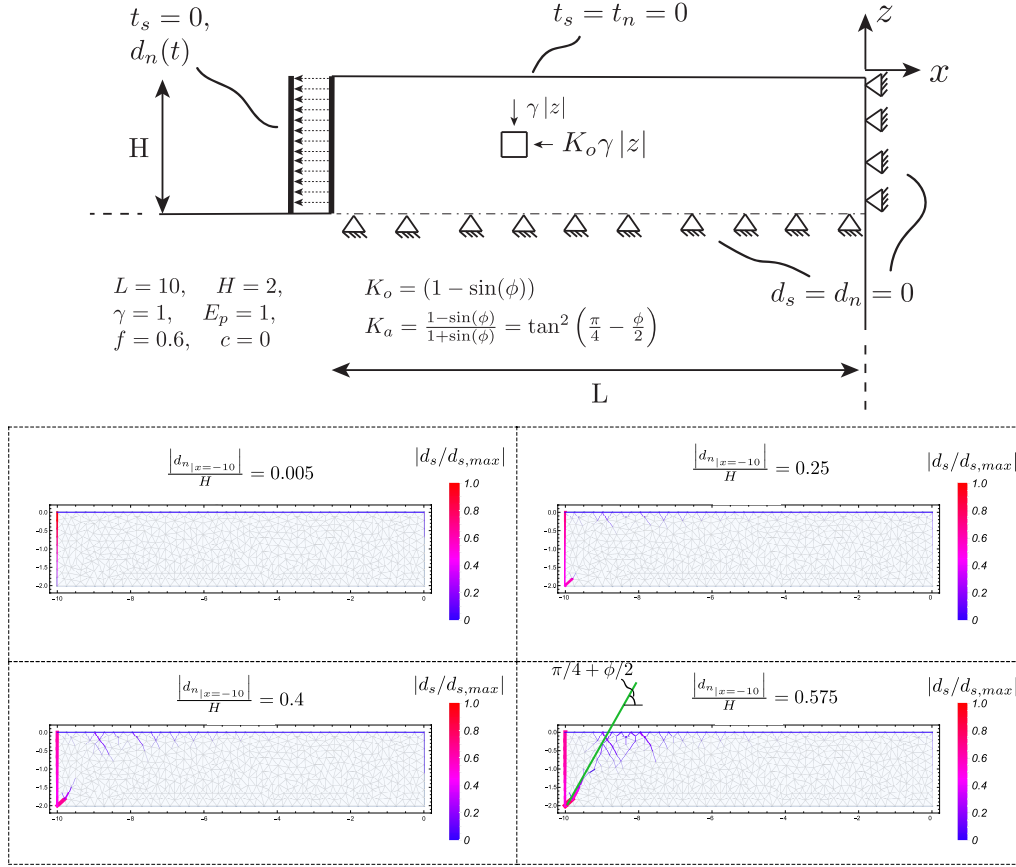


Figure 11: Top: sketch of a retaining wall & boundary conditions adopted. Bottom: evolution of normalized plastic shear deformations $|d_s/d_{s,max}|$ along the pre-existing potential failure segments (unstructured mesh) as a function of normalized translation of the rigid wall $|d_n|_{x=-10}|/H$.

purely frictional material with zero cohesion. At initial conditions, the stress state is given by two compressive principal stresses: the vertical stress $\gamma|z|$ due to the soil weight and the horizontal stress $K_o\gamma|z|$ due to the lateral confinement with $K_o = (1 - \sin(\phi))$ the coefficient of Earth pressure at rest and $\phi = \arctan(f)$ the internal friction angle of the material. The limit active state is reached by reducing the horizontal principal stresses, while keeping the vertical stress constant, until their ratio equals the active Earth pressure

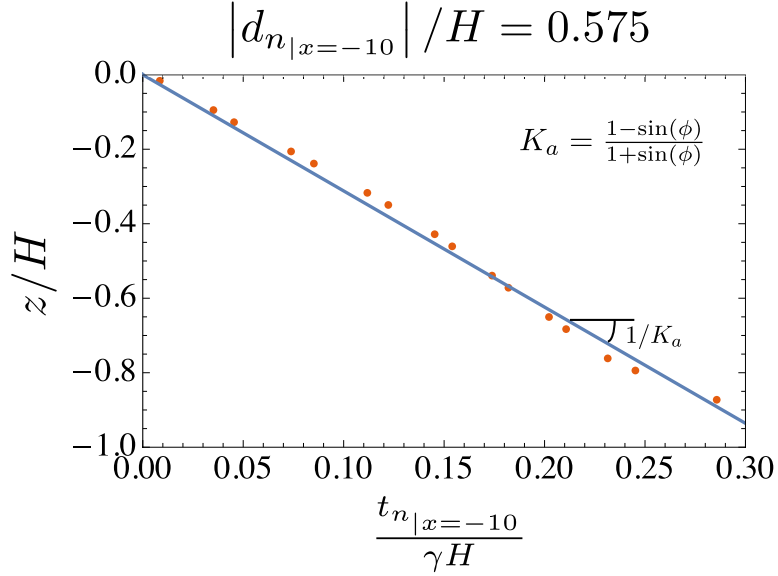


Figure 12: Vertical profile of normalized horizontal stress distribution along the retaining wall (i.e. at $x = -10$) in corresponding of an active limit state. The blue solid line corresponds to the theoretical solution from Rankine theory $\left(K_a = \frac{1 - \sin(\phi)}{1 + \sin(\phi)}\right)$.

coefficient K_a (obtained from Rankine theory [53])

$$K_a = \frac{1 - \sin(\phi)}{1 + \sin(\phi)} = \tan^2\left(\frac{\pi}{4} - \frac{\phi}{2}\right)$$

550 Numerically, this is obtained by translating the rigid wall along the horizontal
 551 direction by prescribing a constant normal displacement discontinuities along
 552 the wall while imposing zero shear stress at the wall (see Figure 11-top for
 553 geometry, input data and boundary conditions of the problem).

554 Figure 11-bottom displays the evolution of cumulative plastic shear deforma-
 555 tions within the soil as function of the normalized lateral displacement of
 556 the wall, until the active state is reached. The progressive decrease of lateral
 557 confinement associated with the translation of the wall leads to progressive
 558 plastic failure that starts to develop from the bottom-left corner, where the
 559 stress concentration is higher, and moves up to the traction free surface. Al-
 560 though the progressive failure path is not straight due to the unstructured
 561 mesh of potential failing segments used, its approximate angle with respect to
 562 the minimum principal direction during active limit state is very close to the

563 theoretical value from Rankine theory $\pi/4 + \phi/2$ (see Figure 11-bottom). The
 564 horizontal stress distribution along the wall is also following the theoretical
 565 prediction $\sigma_{xx} = K_a \sigma_{zz} = K_a(\gamma|z|)$ (see Figure 12).

566 4.5. Fluid injection into a frictional weakening planar fault

567 The numerical solver described in section 3 is capable of solving one-way
 568 coupled hydro-mechanical problems, where the pore-pressure history is ob-
 569 tained from a flow solver. As a first example, we investigate the case of fluid
 570 injection into a frictional weakening planar fault in an infinite and imper-
 571 meable medium. The fault is subjected to an initial uniform effective stress
 572 state with normal and tangential component denoted respectively as σ'_o and
 573 τ_o . In this example, the fault is characterized by a constant longitudinal
 574 permeability k_f . The friction coefficient f of the fault is supposed to soften
 575 linearly with shear slip from a peak value f_p , up to a residual value f_r at
 576 large deformations. Fluid is injected at a point under constant over-pressure
 577 ΔP (above the initial pore pressure p_o) with the purpose of activating slip
 578 upon local violation of the shear weakening Mohr-Coulomb yielding criterion
 579 (no cohesion $c = 0$). This specific problem has been solved by Garagash
 580 and Germanovich [54] semi-analytically. In order to test the accuracy of
 581 our numerical solver with a time-dependent, one-way coupled and non-linear
 582 hydro-mechanical problem, we discretize the fault plane with 10^3 equally-
 583 sized straight segments. We vary the compression of the fully populated
 584 elasticity matrix by using four values of $\eta = 0, 0.1, 0.8, 3$, obtaining respec-
 585 tively compression ratios of $c_r = 1, 0.296, 0.123$ and 0.093 (for $\epsilon_{ACA} = 10^{-4}$
 586 and $n_{leaf} = 16$). Furthermore, we ensure that all the simulations follow the
 587 exact same time-steps evolution so as to calculate a relative difference at
 588 each time step with the results obtained without using a hierarchical matrix
 589 approximation ($\eta = 0$ that we take as reference numerical solution).

590 Figure 13 displays the time evolution of normalized half-crack length (left)
 591 and the peak slip accumulated at the middle of the fault (right), for the case
 592 of a marginally pressurized fault $\tau_o/\tau_p = 0.55$ where $\tau_p = f_p(\sigma_o - p_o) = f_p\sigma'_o$ is
 593 the peak shear strength of the fault at ambient conditions, moderate injection
 594 overpressure $\Delta P/\sigma'_o = 0.5$ and the coarser hierarchical approximation of the
 595 elasticity matrix $\eta = 1$. The numerical results are in very good agreement
 596 with the ones of Garagash and Germanovich [54], both for the evolution of
 597 the shear crack length as well as the peak slip at $x = 0$. The aseismic crack
 598 propagation is followed by the nucleation of a dynamic rupture and an arrest
 599 related to the shear crack catching up the fluid front (see Garagash and

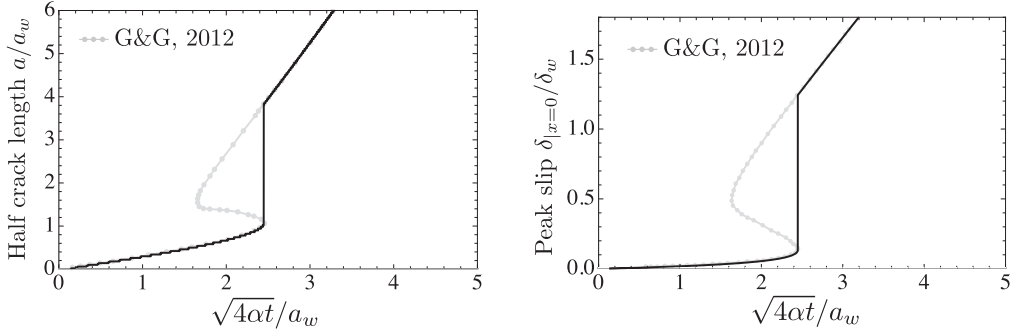


Figure 13: Time evolution of the normalized half-crack length a/a_w (left) and normalized peak slip δ/δ_w at the middle of the fault (right), i.e. at $x = 0$, for an ultimately stable fault ($\tau_o/\tau_p = 0.55$), subjected to a moderate over-pressure $\Delta P/\sigma'_o = 0.5$. a_w and δ_w are the characteristic patch length and slip weakening scale, respectively (see [54] for details). The friction weakening ratio considered is taken here as $f_r/f_p = 0.6$.

600 Germanovich [54] for discussion). This non-trivial evolution is well captured
 601 by our numerical solver. In table 2, we report the maximum relative difference
 602 in terms for the half crack length and peak slip at $x = 0$ obtained during
 603 their time evolution (taking the numerical results for the non-approximated
 604 elasticity matrix as a reference). Even for large compression, the relative error
 605 never exceeds 1.2%, showing a good accuracy and a significant computational
 606 gain. For a GMRES tolerance equal to 10^{-8} , the comparison of total CPU
 607 times (scaled by the total CPU time for the uncompressed case $\eta = 0$),
 608 shows that the use of a hierarchical matrix approximation leads to nearly a
 609 ~ 5 -fold speed-up with respect to the uncompressed case. These results have
 610 been obtained using a C++ implementation of the numerical solver, running
 611 on a computer with Intel Core i5 @ 2.9 GHz.

612 4.6. Fluid injection in a critically stressed fractured rock mass

613 As a final example, we present the case of a hydraulic stimulation of a
 614 fractured rock mass, subjected to a compressive far-field stress state with an
 615 effective principal components denoted by σ'_{xx} and σ'_{yy} (with $\sigma'_{xx} > \sigma'_{yy}$). In
 616 this example, failure can localize only along a set of 251 randomly oriented
 617 pre-existing fractures, which are uniformly located within the region of inter-
 618 est $L \times L$. We adopt a power law distribution for fracture length generation
 619 with cut-off for minimum and maximum fracture lengths. This choice has
 620 been demonstrated in numerous studies at different scales and in different
 621 tectonic setting [55, 56].

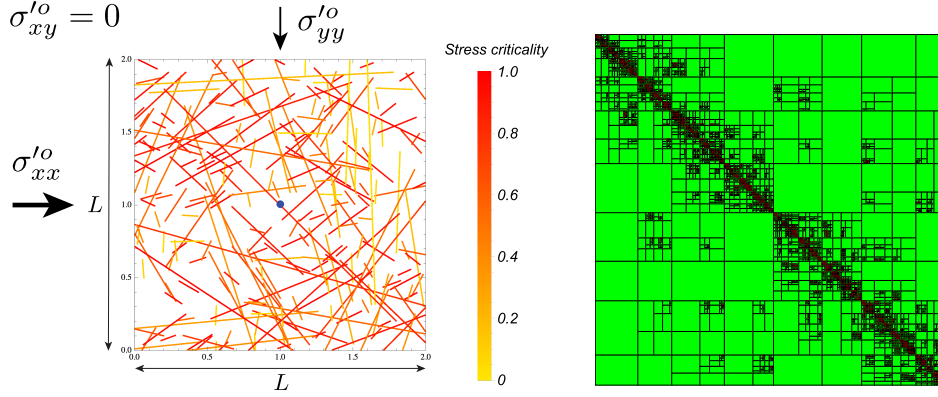


Figure 14: Left: critically stressed discrete fracture network. The color of each fracture denotes the stress criticality Λ at ambient condition. Right: hierarchical matrix pattern upon compression (with $\eta = 3$, $\epsilon_{ACA} = 10^{-6}$ and $n_{leaf} = 100$) with low-rank block in green.

622 Upon generation of 251 pre-existing fractures within the elementary area
 623 of characteristic size L (see Figure 14-left) and discretization with 11376
 624 straight segments resulting in a total of $\sim 10^5$ unknowns, fluid is injected
 625 at $(L/2; L/2)$ under a constant injection over-pressure ΔP (in excess of the
 626 initial pore pressure p_o) such that it always remain below the minimum prin-
 627 cipal effective normal stress (to avoid tensile opening of any fractures). We
 628 assume that the permeability of the host medium is much smaller than the
 629 one of the fracture such that the fluid flow only within the pre-existing frac-
 630 tures (characterized by constant hydraulic diffusivity α). The fluid flow is
 631 solved via a finite volume solver - uncoupled here to the mechanical deforma-
 632 tion. The pre-existing fractures exhibit a purely frictional behavior with zero
 633 cohesion and without any softening (constant friction coefficient $f = 0.6$).

634 We scale all the spatial variables with $L/2$, which is the minimum dis-
 635 tance that the fluid front can 'travel' before reaching the boundary of the
 636 region of interest (supposing that fluid is injected at $(L/2; L/2)$) and the
 637 time t with the characteristic fluid diffusion timescale $L^2/(16\alpha)$. The char-
 638 acteristic scales for fluid over-pressure $\Delta p = (p - p_o)$ and effective tractions
 639 t'_i are respectively the in-situ effective normal traction $t'_{n,o}{}^{k_{inj}}$ and the peak
 640 shear strength $t'_{s,p}{}^{k_{inj}} = f \cdot t'_{n,o}{}^{k_{inj}}$ of the fracture in which fluid is injected into,
 641 while shear slip is scaled using the characteristic scale $d_{s,w} = \frac{t'_{s,p}{}^{k_{inj}} L}{E' 2}$ that de-
 642 rives from elasticity. Upon scaling the governing equations with the previous

643 characteristic scales, the solution given by $(p - p_p)/t'_{n,o}, t'_i/t'_{s,p}, d_s/d_{s,w}$ is
 644 function of (besides the geometry of the pre-existing fractures network) two
 645 dimensionless parameters: i) a stress criticality ratio

$$\Lambda = \frac{(\kappa - 1)}{f} \frac{\text{Cot}(\theta)}{(\kappa \text{Cot}(\theta)^2 + 1)}, \quad (32)$$

646 which is function of effective stress anisotropy ratio $\kappa = \frac{\sigma'_{xx}}{\sigma'_{yy}}$, friction coeffi-
 647 cient f and local fracture orientation θ with respect to the minimum principal
 648 direction, and ii) normalized injection over-pressure at fracture k_{inj} in which
 649 fluid is injected into

$$\Pi = \frac{\Delta P}{t'_{n,o} k_{inj}}, \quad (33)$$

650 where $t'_{n,o}$ is the uniform ambient effective normal stress along the fracture
 651 k_{inj} . Because of the relatively large effective stress anisotropy ratio $\kappa = 3$
 652 used in this example, all the pre-existing fractures oriented along the critical
 653 angle $\theta_c = \pi/4 + \phi/2$ are critically stressed (see Figure 14-left). They are
 654 prompt to fail with little pressurization.

655 Due to the large number of unknowns, we use a hierarchical approxi-
 656 mation of the elasticity matrix using $\eta = 3$, $\epsilon_{ACA} = 10^{-6}$, $n_{leaf} = 100$
 657 resulting in a a compression ratio of $c_r = 0.0751$, sufficient to be able to run
 658 the simulation with a 2.9 GHz Intel Core i5 laptop with 8 GB memory (see
 659 the pattern of hierarchical matrix in Figure 14-right).

660 As one can see from Figure 15 that displays the normalized over-pressure
 661 and shear rupture evolution in function of normalized time/fluid front po-
 662 sition, right after fluid injection the slipping patch evolves rapidly, much
 663 faster than fluid diffusion front. As the slipping patch propagates, the stress
 664 state changes within the elementary area, activating other fractures. At a
 665 normalized time $\frac{\sqrt{4\alpha t}}{L/2} \simeq 0.37$, the pressurized zone is still confined to the
 666 surrounding of the injection point, while the slipping patch is significantly
 667 larger. The slipping patch evolution is thus mainly driven by stress interac-
 668 tion between active fractures.

669 The numerical solver devised captures well the yielding evolution driven
 670 by fluid flow and elastic stress interactions between activated pre-existing
 671 fractures. That example with $\sim 10^5$ degrees of freedom demonstrates the
 672 robustness of the preconditioning developed in section 3. The number of

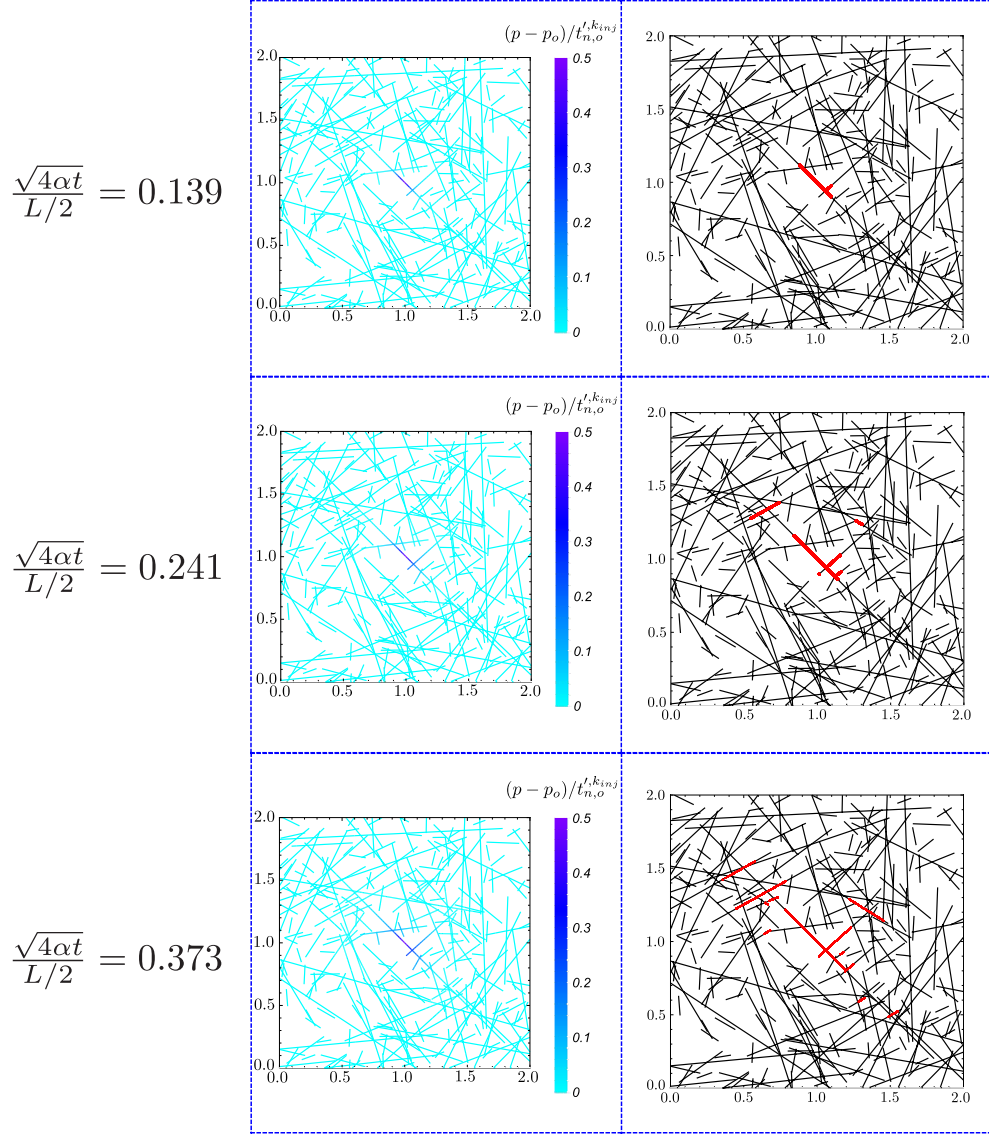


Figure 15: Evolution of normalized over-pressure (left column) and plasticity localization (shear deformations - right column) along the pre-existing critically stressed fracture network in function of normalized time/fluid front position $\frac{\sqrt{4\alpha t}}{L/2}$. Fluid is injected at moderate over-pressure $\Delta P/t_{n,o}^{k_{inj}} = 0.5$ into one fracture that intersect the injection point located at (1, 1).

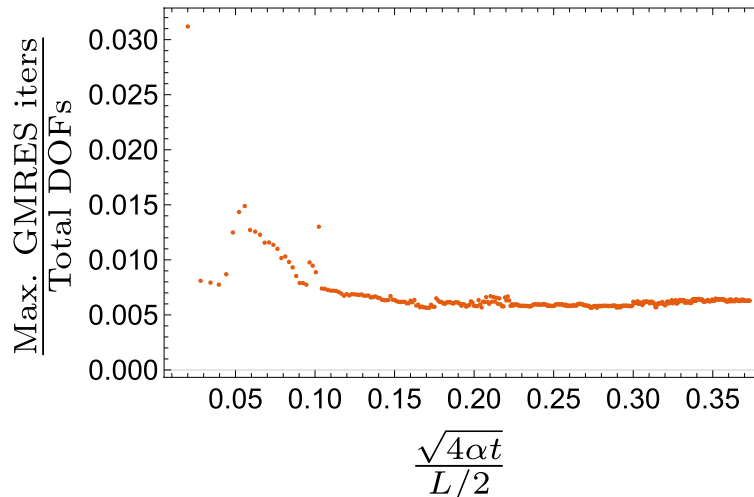


Figure 16: Maximum number of GMRES iterations required to solve the mechanical problem at each time step. A convergence tolerance $tol = 10^{-6}$ was used for the GMRES iterative solver.

673 iterations (scaled by the number of unknowns) for the GMRES iterative
 674 solver remains below 1.5% for all time steps as can be seen in Figure 16.

675 5. Conclusions

676 We have presented a new boundary element based formulation for in-
 677 elastic localized deformation along potential pre-existing failure planes. The
 678 Mohr-Coulomb criteria combined with a tensile cut-off and the linear soften-
 679 ing laws used here can easily be replaced by more refined constitutive models
 680 if necessary. The efficiency of the numerical scheme devised rely on the use
 681 of i) a hierarchical approximation of the elastic influence matrix and ii) a
 682 block pre-conditioner specifically developed here. The proposed computa-
 683 tional method shares similarities with the intrinsic cohesive zone element
 684 approach used in the FEM context where cohesive elements are activated
 685 upon yielding at the interfaces between finite elements [18, 19, 10]. However,
 686 the use of a boundary element method allows to decouple the discretization
 687 of the failure plane and the rest of the medium (whose elasticity is built-in
 688 BEM). This is particularly attractive for problems in infinite domain as well
 689 as cases where deformation is strongly localized into a finite number of shear
 690 bands or cracks. The approach is also advantageous when fluid flow and me-

691 chanical deformation are coupled such as for hydraulic fracturing problems
692 [57]. With respect to the hydro-mechanical behavior of fractured rocks, it
693 would be interesting to further compare the approach proposed here (which
694 explicitly model all discontinuities) with continuum non-local microstructural
695 brittle damage models [58, 59].

696 The different examples reported demonstrate the versatility of the pro-
697 posed approach in dealing with various problems exhibiting localized plastic
698 deformation as well as crack growth. Unlike others existing BEM or FEM for-
699 mulations for inelastic problems based on bulk plasticity with softening, this
700 numerical scheme does not show mesh dependency as long as the softening
701 length-scale is properly resolved and -more importantly- that the true plane
702 of localized deformations are discretized (in other words known a-priori).
703 This last point can be fixed by modifying/refining the discretization of the
704 initial DD segments in an adaptive manner according to a measure of inelastic
705 deformation (e.g. shear dissipation) averaged in the bulk. Another possible
706 extension of the proposed algorithm is to move to an approach where new DD
707 elements are added in the proper direction to capture the plane of localized
708 deformation as it progresses. Such an algorithm would require to search iter-
709 atively for direction of failure advancement ahead of the shear-bands/cracks
710 using a similar yielding criteria.

711 **Acknowledgements**

712 This work was funded by the Swiss National Science Foundation (grant
713 160577) and the Swiss Federal Office of Energy (grant S/I 50135401).

714 **Authors contributions**

715 Federico Ciardo: Conceptualization, Methodology, Formal analysis, In-
716 vestigation, Software, Visualization, Validation, Writing – original draft

717 Brice Lecampion: Conceptualization, Methodology, Formal analysis, In-
718 vestigation, Writing – review & editing, Supervision

719 François Fayard: Investigation, Software, Validation

720 Stéphanie Chaillat: Conceptualization, Software, Writing – review & edit-
721 ing

722 **References**

- 723 [1] A. Needleman, A numerical study of necking in circular cylindrical bars,
724 J. Mech. Phys. Solids 20 (1972) 111–127.
- 725 [2] A. Needleman, V. Tvergaard, Necking of biaxially stretched elastic-
726 plastic circular plates, J. Mech. Phys. Solids 25 (1977) 159–183.

- 727 [3] V. Tvergaard, A. Needleman, K. K. Lo, Flow localization in the plane
728 strain tensile test, *J. Mech. Phys. Solids* 29 (1981) 15–142.
- 729 [4] T. Belytschko, J. Fish, B. E. Engelmann, A finite element with embed-
730 ded localization zones, *Computer methods in applied mechanics and*
731 *engineering* 70 (1988) 59–89.
- 732 [5] D. Bigoni, D. Capuani, Green’s function for incremental nonlinear elas-
733 ticity: shear bands and boundary integral formulation, *Journal of the*
734 *Mechanics and Physics of Solids* 50 (2002) 471–500.
- 735 [6] M. Brun, D. Bigoni, D. Capuani, A boundary element technique for
736 incremental, non-linear elasticity - Part II: Bifurcation and shear bands,
737 *Computer methods in applied mechanics and engineering* 192 (2003)
738 2481–2499.
- 739 [7] M. Bonnet, *Boundary Integral Equation Methods for Solids and Fluids*,
740 John Wiley & Sons, 1999.
- 741 [8] J. Rice, The localization of plastic deformation, in: W. Koiter (Ed.), *14th*
742 *International Congress on Theoretical and Applied Mechanics*, North-
743 *Holland, Amsterdam, 1977*, pp. 207–220.
- 744 [9] A. Needleman, Material rate dependence and mesh sensitivity in local-
745 ization problems, *Computer methods in applied mechanics and engi-*
746 *neering* 67 (1988) 69–85.
- 747 [10] F. Zhou, J.-F. Molinari, T. Shioya, A rate-dependent cohesive model for
748 simulating dynamic crack propagation in brittle materials, *Engineering*
749 *Fracture Mechanics* (2005) 1383–1410.
- 750 [11] A. Benallal, C. A. Fudoli, W. S. Venturini, An implicit BEM formulation
751 for gradient plasticity and localization phenomena, *International journal*
752 *for numerical methods in engineering* 53 (2002) 1853–1869.
- 753 [12] H.-B. Mühlhaus, E. C. Aifantis, A variational principle for gradient
754 plasticity, *Int. J. Solids Structures* 28 (1991) 845–857.
- 755 [13] R. De Borst, H.-B. Mühlhaus, Gradient-dependent plasticity: formula-
756 tion and algorithm aspects, *Internatioan journal for numerical methods*
757 *in engineering* 35 (1992) 521–539.

- 758 [14] A. Benallal, A. Botta, W. S. Venturini, On the description of localization
759 and failure phenomena by the boundary element method, *Computer*
760 *methods in applied mechanics and engineering* 195 (2006) 5833–5856.
- 761 [15] R. De Borst, Simulation of strain localisation: a reappraisal of the
762 Cosserat continuum, *Engineering computations* 8 (1991) 317–332.
- 763 [16] X.-P. Xu, A. Needleman, Numerical simulations of fast crack growth in
764 brittle solids, *Journal of the Mechanics and Physics of Solids* 42 (1994)
765 1397–1434.
- 766 [17] G. T. Camacho, M. Ortiz, Computational modelling of impact damage
767 in brittle materials, *Int. J. Solids Structures* 33 (1996) 2899–2938.
- 768 [18] A. Pandolfi, M. Ortiz, An efficient adaptive procedure for three-
769 dimensional fragmentation simulations, *Engineering with computers* 18
770 (2002) 148–159.
- 771 [19] F. Zhou, J.-F. Molinari, Dynamic crack propagation with cohesive ele-
772 ments: a methodology to address mesh dependency, *International jour-
773 nal for numerical methods in engineering* 59 (2004) 1–24.
- 774 [20] A. C. Palmer, J. Rice, The growth of slip surfaces in the progressive
775 failure of over-consolidated clay, in: *Proceedings of the Royal Society*
776 *of London A: Mathematical, Physical and Engineering Sciences*, volume
777 332, The Royal Society, pp. 527–548.
- 778 [21] E. Van der Giessen, A. Needleman, Discrete dislocation plasticity: a
779 simple planar model, *Modelling and Simulation in Materials Science*
780 *and Engineering* 3 (1995) 689–735.
- 781 [22] G. Maier, G. Novati, Z. Chen, Symmetric galerkin boundary element
782 method for quasi-brittle-fracture and frictional contact problems, *Com-
783 putational Mechanics* 13 (1993) 74–89.
- 784 [23] D. A. Hill, P. A. Kelly, D. N. Dai, A. M. Korsunsky, *Solution of Crack*
785 *Problems: the Distributed Dislocation Technique*, Kluwer Academic
786 Publishers, 1996.
- 787 [24] S. G. Mogilevskaya, Lost in translation: Crack problems in different
788 languages, *International Journal of Solids and Structures* 51 (2014)
789 4492–4503.

- 790 [25] S. L. Crouch, A. M. Starfield, *Boundary Element Methods in Solid Me-*
791 *chanics*, George Allen and Unwin, 1983.
- 792 [26] M. Bonnet, G. Maier, C. Polizzotto, Symmetric galerkin boundary ele-
793 *ment methods*, *Applied Mechanics Reviews* 51 (1998) 669–704.
- 794 [27] Itasca Consulting Group, *FLAC Constitutive models*, Technical report,
795 Itasca Consulting Group, 2010.
- 796 [28] F. Ciardo, B. Lecampion, Effect of dilatancy on the transition from
797 aseismic to seismic slip due to fluid injection in a fault, *Journal of*
798 *Geophysical Research: Solid Earth* 124 (2019) 3724–3743.
- 799 [29] S. Stupkiewicz, Z. Mróz, Modelling of friction and dilatancy effects at
800 brittle interfaces for monotonic and cyclic loading, *Journal of theoretical*
801 *and applied mechanics* 3 (2001).
- 802 [30] M. Ortiz, A. Pandolfi, Finite-deformation irreversible cohesive elements
803 for three-dimensional crack-propagation analysis, *International journal*
804 *for numerical methods in engineering* 44 (1999) 1267–1282.
- 805 [31] L. Snozzi, J.-F. Molinari, A cohesive element model for mixed mode
806 loading with frictional contact capability, *International journal for nu-*
807 *merical methods in engineering* 93 (2013) 510–526.
- 808 [32] A. Crawford, J. Curran, Higher-order functional variation displacement
809 discontinuity elements, *International Journal of Rock Mechanics and*
810 *Mining Science & Geomechanics Abstracts* 19 (1982) 143–148.
- 811 [33] W. Hackbusch, A Sparse Matrix Arithmetic Based on \mathcal{H} -Matrices. Part
812 I: Introduction to \mathcal{H} -Matrices., *Computing* 62 (1999) 89–108.
- 813 [34] W. Hackbusch, *Hierarchical matrices: algorithm and analysis*, vol-
814 *ume 49*, Springer, 2015.
- 815 [35] M. Bebendorf, *Hierarchical matrices: A Means to Efficiently Solve El-*
816 *liptic Boundary Value Problems*, Springer, 2008.
- 817 [36] S. Chaillat, L. Desiderio, P. Ciarlet, Theory and implementation of
818 h-matrix based iterative and direct solvers for helmholtz and elastody-
819 *amic oscillatory kernels*, *Journal of Computational Physics* 351 (2017)
820 165–186.

- 821 [37] A. Quarteroni, R. Sacco, F. Saleri, Numerical mathematics, Springer,
822 2000.
- 823 [38] M. Benzi, G. H. Golub, J. Liesen, Numerical solution of saddle point
824 problems, *Acta Numerica* (2005) 1–37.
- 825 [39] Z.-H. Cao, Augmentation block preconditioners for saddle point-type
826 matrices with singular (1,1) blocks, *Numerical linear algebra with ap-
827 plications* 15 (2008) 515–533.
- 828 [40] Z.-H. Cao, Constraint Schur complement preconditioners for nonsym-
829 metric saddle point problems, *Applied Numerical Mathematics* 59
830 (2009) 151–169.
- 831 [41] J.-L. Li, T.-Z. Huang, L. Li, The spectral properties of the precon-
832 ditioned matrix for nonsymmetric saddle point problems, *Journal of
833 Computational and Applied Mathematics* 235 (2010) 270–285.
- 834 [42] S. Li, S. Ahmed, G. Klimeck, E. Darve, Computing entries of the inverse
835 of a sparse matrix using the FIND algorithm, *Journal of Computational
836 Physics* 227 (2008) 9408–9427.
- 837 [43] A. M. Erisman, W. F. Tinney, On computing certain elements of the
838 inverse of a sparse matrix, *Numerical mathematics* (1975).
- 839 [44] F. Maerten, L. Maerten, M. Cooke, Solving 3D boundary element prob-
840 lems using constrained iterative approach, *Computational Geoscience*
841 14 (2010) 551–564.
- 842 [45] M. L. Cooke, D. D. Pollard, Bedding-plane slip in initial stages of fault-
843 related folding, *Journal of Structural Geology* 19 (1997) 567–581.
- 844 [46] G. Kirsch, *Die Theorie der Elastizität und die Bedürfnisse der Festigkeit-
845 lehre*, Springer, 1898.
- 846 [47] B. Lecampion, Modeling size effects associated with tensile fracture
847 initiation from a wellbore, *International Journal of Rock Mechanics and
848 Mining Science* 56 (2012) 67–76.
- 849 [48] D. Leguillon, D. Quesada, C. Putot, E. Martin, Prediction of crack
850 initiation at blunt notches and cavities: size effects, *Eng. Frac. Mech.*
851 74 (2007) 2420–2436.

- 852 [49] J. W. Rudnicki, J. R. Rice, Conditions for the localization of deformation
853 in pressure-sensitive dilatant materials, *J. Mech. Phys. Solids* 23 (1975)
854 371–394.
- 855 [50] J. Rice, The localization of plastic deformation, *Theoretical and Applied*
856 *Mechanics* (Proceeding of the 14th International Congress on Theoret-
857 ical and Applied Mechanics, Delft, 1976, ed. W. T. Koiter) 1 (1976)
858 207–220.
- 859 [51] M. Ortiz, Y. Leroy, A. Needleman, A finite element method for lo-
860 calized failure analysis, *Computer methods in applied mechanics and*
861 *engineering* 61 (1987) 189–214.
- 862 [52] F. Armero, K. Garikipati, An analysis of strong discontinuities in muti-
863 plicative finite strain plasticity simulation of strain localization in solids,
864 *Int. J. Solids Structures* 33 (1996) 2863–2885.
- 865 [53] K. Terzaghi, *Theoretical soil mechanics*, John Wiley & Sons, 1943.
- 866 [54] D. I. Garagash, L. N. Germanovich, Nucleation and arrest of dynamic
867 slip on a pressurized fault, *Journal of Geophysical Research* 117 (2012).
- 868 [55] C. G. Hatton, I. G. Main, P. G. Meredith, Non-universal scaling of
869 fracture length and opening displacement, *Nature* 367 (1994).
- 870 [56] R. L. Kranz, Microcracks in rocks: a review, *Tectonophysics* 100 (1983)
871 449–480.
- 872 [57] B. Lecampion, A. P. Bungler, X. Zhang, Numerical methods for hydraulic
873 fracture propagation: A review of recent trends, *Journal of Natural Gas*
874 *Science and Engineering* 49 (2018) 66–83.
- 875 [58] M. De Bellis, G. Della Vecchia, M. Ortiz, A. Pandolfi, A lin-
876 earized porous brittle damage material model with distributed frictional-
877 cohesive faults, *Engineering Geology* 215 (2016) 10–24.
- 878 [59] M. L. De Bellis, G. Della Vecchia, M. Ortiz, A. Pandolfi, A multiscale
879 model of distributed fracture and permeability in solids in all-round
880 compression, *Journal of the Mechanics and Physics of Solids* 104 (2017)
881 12–31.

\mathcal{I}	0.1	1	10
$p_b/p_{b,\text{strength}}$	1.052	1.448	2.906
$p_b/p_{b,\text{strength}}$ from [47]	~ 1.1	~ 1.45	~ 2.9

Table 1: Comparison of the normalized crack initiation pressure obtained here and the ones of Lecampion [47] for different Irwin numbers \mathcal{I} .

	$\eta = 0.1$	$\eta = 0.8$	$\eta = 3$
Compression ratio c_r	0.296	0.123	0.093
Scaled total CPU time	0.688	0.276	0.213
Max. rel. difference on half crack length	$0.5 \cdot 10^{-3}$	$1.5 \cdot 10^{-3}$	$1.2 \cdot 10^{-2}$
Max. rel. difference on peak slip	$1.49 \cdot 10^{-6}$	$1.48 \cdot 10^{-6}$	$3.96 \cdot 10^{-5}$

Table 2: Scaled total CPU time and the maximum relative difference obtained during the simulation for different values of η for the hierarchical approximation. The reference numerical solution corresponds to the $\eta = 0$ case (no compression of the elasticity matrix).